This is a preprint, the final version is subject to change, of the American Mineralogist (MSA)
Cite as Authors (Year) Title. American Mineralogist, in press.
DOI: https://doi.org/10.2138/am-2020-7061

Revision 2

The role of clay minerals in forming the regolith-hosted heavy rare earth element deposits

Martin Yan Hei Li, Mei-Fu Zhou*

Department of Earth Sciences, The University of Hong Kong, Pokfulam Road, Hong Kong

---

*Corresponding author:

Mei-Fu Zhou

Email: mfzhou@hku.hk

Tel: (+852)28578251

Fax: (+852)25176912

Abstracts

Rare earth elements (REEs) have become increasingly important to our modern society due to their strategical significance and numerous high-technological applications. Regolith-hosted HREE deposits in South China are currently the main source of the heavy REEs (HREEs) but the ore-forming processes are poorly understood. In these deposits, the REEs are postulated to accumulate in regolith through adsorption on clay minerals. In the Zudong deposit, the world's largest regolith-hosted HREE deposit, clay minerals are dominated by short, stubby, nm-scale halloysite tubes (either of 10Å or 7Å) and microcrystalline kaolinite in the saprolite and lower pedolith and μm-sized vermicular kaolinite in the humic layer and upper pedolith. A critical transformation of the clay minerals in the upper pedolith is coalescence and unrolling of halloysite to form vermicular kaolinite. Microcrystalline kaolinite also transformed to large, well-crystalline vermicular kaolinite. This transformation could result in significant changes in different physicochemical properties of the clay assemblages. Halloysite-abundant clay assemblages in the deep regolith have specific surface area and porosity significantly higher than the kaolinite-dominant clay assemblages in the shallow soils. Crystallinity of clay minerals also increased, exemplified by decrease in Fe contents of the kaolinite group minerals (from ~1.2 wt. % in the lower saprolite to ~0.35 wt. % in the upper pedolith), thereby indicative of less availability of various types of adsorption sites. Hence, halloysite-abundant clay minerals of high adsorption capacity in deep regolith could efficiently retain the REEs released from weathering of the parent granite. Reduction in adsorption capacity during the clay

transformation in shallow depth partially leads to REE desorption, and the released REEs would be subsequently transported to and adsorbed at deeper part of the soil profile. Hence, the clay-adsorbed REE concentration in the lower pedolith and saprolite (~2,500 ppm on average) is much higher than the uppermost soils (~400 ppm on average). Therefore, weathering environments that favor the release of the REEs in the shallow soils but preservation of halloysite in the deep regolith can continuously adsorb REEs in the clay minerals to form economically valuable deposits.

Key words: Rare earth elements (REEs), REE adsorption, halloysite, kaolinite, regolith-hosted REE deposits, weathering

Introduction

In facing a continuously growing demand of the rare earth elements (REEs) for various high-technological applications in our modern society, REE resources have become a popular exploration target in the world, especially for the more scarce but important heavy REEs (HREEs). Currently, regolith-hosted HREE deposits are the dominant source of the global HREE production (Simandl, 2014). These deposits are characterized by low grades (0.05 - 0.2 wt.% rare earth oxide; REO) and individually small tonnages (<10 kt REO resources), except the super-large Zudong deposit (Li et al., 2017; Xie et al., 2016). They formed through mobilization, circulation and accumulation of the REEs in regolith, mostly developed from granites and associated volcanic rocks (Li et al., 2017; Sanematsu and Watanabe, 2016). Such deposits occur mostly in South China and other sub-tropical and tropical localities, including the Southeast Asia, Madagascar, Malawi, and Brazil (Berger et al., 2014; Li et al., 2017; Sanematsu and Watanabe, 2016). Accumulation of the REEs in these deposits is postulated to the REE adsorption on various clay minerals as weakly bound outer sphere complexes (Yamaguchi et al., 2018). This explains the feasibility of low-cost extraction through chemical leaching by dilute electrolyte solutions (Moldoveanu and Papangelakis, 2016).

Albeit the importance of clay minerals in accumulating the REEs, most previous studies dealt with bulk mineralogy and geochemistry of these deposits (e.g. Bao and Zhao, 2008; Berger et al., 2014; Padrones et al., 2017; Sanematsu et al., 2015; Sanematsu et al., 2013; Wu et al., 1990). Some recent studies have considered and examined size fractionation of the REEs

(Cheshire, 2011; Cheshire et al., 2018; Elliott et al., 2018), nonetheless, detailed investigations on the clay-sized particles are still lacking. It has been demonstrated that the REEs concentrate in the lower pedolith (B horizon) and upper saprolite (C horizon). The interface between the pedolith and saprolite could be considered as a significant weathering front. Here, consumption of the saprolitic materials to form the pedolith usually leaves behind only residual phases, including refractory REE-bearing minerals, causing an apparent REE accumulation. More importantly, a large amount of the REEs accumulates very likely due to adsorption on the clay minerals. In these deposits, kaolinite and halloysite are frequently observed, whereas occurrence of smectite and illite are usually rare and confined only to the lower part of soil profiles (Li et al., 2019; Wu et al., 1990). However, the role of clay minerals is still poorly understood and little is known about the relationship between species, modes of occurrence, and abundance of clay minerals and REE adsorption. Here, we choose the world's largest Zudong regolith-hosted HREE deposit, and focus on the variation and transformation of clay minerals in progressive weathering and the associated changes in various physicochemical properties. Thereby, we explore the role of clay minerals in mobilizing and accumulating REEs in regolith to constrain the origin of regolith-hosted HREE deposits.

Site description

The Zudong deposit in southern Jiangxi province (Fig. 1) is HREE-dominant with a current total resource of 17,622 t (pre-mining estimate of 131,000 t at 0.048 wt. % REO) of

REO with an average grade of ~0.1 wt. % REO (Li et al., 2019; Xie et al., 2016). Regionally, the Zudong deposit is located on a moderately undulating landform, with elevation varying from ~250 to 500 m above sea level and slope gradients from 10º to 15º (Liu et al., 2016), and subjected to a subtropical monsoon climate with annual rainfall of 1,200 - 1,900 mm (Huang et al., 2013).

Thicknesses of soil profiles in the deposit range generally from a few meters to 30 m from field observation. A clear soil zonation can be observed, and includes from top to bottom a surficial humic layer (A horizon, 0 - 1 m thick), a pedolith (B horizon, 1 - 10 m thick), and a saprolite zone (C horizon, 3 - 20 m thick) (Fig. 2a). The humic layer is generally dark brownish in appearance with a high total organic carbon (TOC) content. Whereas the pedolith is orangish brown in appearance, attributed to the accumulation of Fe oxyhydroxides (Fig. 2b - c). The soil order could be classified as Ultisol. This zone also contains abundant rounded residual grains of quartz but primary feldspar and muscovite are rare. In the saprolite, relict granitic texture is still largely preserved and exhibits a whitish to pinkish white appearance due to the growth of various clay minerals (Fig. 2d - f). The HREE orebodies, varying from a few meters to up to 10 m thick, exclusively occur in the lower pedolith to upper saprolite (Fig. 2a) (Li et al., 2019). Previous studies have recognized the dominant clay species of kaolinite and halloysite in the soil profiles, with a sub-ordinate amount of illite and smectite in the lower saprolite (Li et al., 2019; Wu et al., 1990). Quantitatively, there are about 10 - 15% kaolinite group minerals in the saprolite and pedolith, but their contents abruptly reach more than 25% in the humic layer (Fig.

3) (Li et al., 2019). Fe-Mn oxyhydroxides and gibbsite are comparatively scarce, even in the uppermost part of the soil profiles (Li et al., 2019; Wu et al., 1990). Supergene REE minerals, including chernovite-(Y) and cerianite-(Ce), and residual REE minerals, such as zircon, xenotime-(Y), and euxenite-(Y), also commonly appear in the soils. It is estimated that these supergene and residual minerals host up to 30% of the total REE contents of the ores, while the remaining ~70% is largely adsorbed on the clay minerals (Li et al., 2019). This deposit formed from weathering of the late Jurassic A-type Zudong granite (zircon U-Pb age of 168 Ma; Zhao et al. (2014)). The major rock-forming minerals include quartz, albite, orthoclase, and muscovite (Fig. 2g). REE concentrations of the parent granite vary from ~200 to 400 ppm with various REE-bearing accessory phases, including synchysite-(Y), gadolinite-(Y), hingganite-(Y), yttrialite-(Y), Y-rich fluorite, xenotime-(Y), euxenite-(Y), fergusonite-(Y), zircon, and thorite. Preferential weathering of some of these minerals, notably synchysite-(Y), gadolinite-(Y), hingganite-(Y), and yttrialite-(Y), supplies most of the REEs to be accumulated in the regolith through continuous circulation. In term of geochemistry, Li et al. (2019) has demonstrated that the soil pH gradually increases from 4.74 in the uppermost humic layer and upper pedolith to ~5.5 in the lower pedolith and upper saprolite, and further to ~6 in the lower saprolite (Table 1). Whereas the REE concentration increases from ~400 ppm in the uppermost humic layer and upper pedolith to more than 1,000 ppm in the ore bodies. Similar trend could be observed for the extractable REE concentrations. The extractable REE concentration increases from ~200 ppm on average in the humic layer and upper pedolith, being ~45% of the

bulk content, to 600 - 700 ppm in the orebody at the lower pedolith and upper saprolite, sharing 60 - 65% of the bulk content (Table 1; Fig. 3). The proportions of the REEs sorbed to Fe-Mn oxyhydroxides are minimal at the Zudong deposit, sharing only ~2% of the total REE contents (Table 1; Fig. 3). The proportions bound to organic substances are negligible (Table 1; Fig. 3).

Sampling and analytical methods

Sampling and sample preparation

Representative samples from different soil horizons of the Zudong deposit were collected at a depth of at least 50 cm deep below the exposed surfaces to avoid anthropogenic effects. Detailed description of the ore deposit and investigation of bulk geochemistry are available in Li et al. (2019). As clay minerals in the studied site could be much larger than 2 μm in size (see results below), particles with size <20 μm were targeted and extracted and further divided into <2 and 2 - 20 μm fractions. To extract the different clay fractions, samples were first suspended in DI water by vigorous shaking and ultrasonic bathed for ~15 mins. Both <2 and <20 μm fraction was collected through sedimentation after required times according to the Stoke's law have lapsed.

Particle size distribution

Particle size distribution was analyzed with a LS I3 320 Laser Diffraction Particle Size Analyzer (PSA) at the Department of Earth Sciences, the University of Hong Kong (HKU). The detection range is 0.2 - 2,000 μm and the error for repeated measurement is <1%.

Scanning electron microscopy (SEM)

Micro- to nano-scale observations were carried out with a Hitachi S-4800 FEG scanning electron microscope (SEM) at the Electron Microscope Unit (EMU), HKU. Operating voltage is 15 kV and samples were coated with carbon before observation. The SEM used is equipped with an Oxford energy-dispersive spectrometer (EDS) for quick semi-quantitative elemental analysis of the clay minerals.

High-resolution transmission electron microscopy (HRTEM)

High-resolution transmission electron microscopic (HRTEM) images were obtained with the Tecnai G2 20 S-TWIN scanning transmission electron microscope at the EMU, HKU operating at an accelerating voltage of 200 kV. Specimens were first dispersed in ethanol and a drop of the suspension was transferred onto a porous carbon film supported by a copper grid. Observations were undertaken after the ethanol had evaporated. Fast Fourier Transform (FFT) processing is applied to obtain the d-spacings of lattice.

X-ray diffraction (XRD)

XRD patterns were collected from 3° to 30° (2θ) for oriented and ethylene glycol-solvated samples, and 3° to 15° (2θ) for 550ºC heated, and K-acetate-and ethylene glycol-solvated samples at a scanning rate of 1º (2θ) min^{-1} on a Rigaku D/max diffractometer with Ni-filtered CuKα radiation (λ = 0.154 nm, 40 kV and 100 mA). Oriented samples were prepared by carefully pipetting the clay suspension onto a glass slide and allowing it to dry at ambient temperature. Ethylene glycol-solvated samples were then prepared by treating the oriented samples in a glass desiccator and solvated with ethylene glycol vapor at 30°C for 24 h, and subsequently heated at 550°C for more than 2.5 h to prepare the heated samples. To further decipher kaolinite and halloysite, K-acetate treatment (Wada, 1961) with additional solvation of ethylene glycol (Miller and Keller, 1963) was adopted. Samples were first soaked in K-acetate and then washed with ethylene glycol. Halloysite has basal spacing in the range of 10 - 11Å, whereas kaolinite retains its original basal spacing of ~7Å after the treatment. The corresponding relative proportions could be determined by computing the $I_{10}/(I_7 + I_{10})$ ratio from the XRD spectra, in which I_7 and I_{10} denote the intensity peaks near 7 and 10Å, respectively. The crystallinity of the kaolinite group minerals is evaluated by the Hinckley Index after Hinckley (1962). The indices are calculated by dividing the sum of the heights of the $1\bar{1}0$ and the $11\bar{1}$ peaks above a line drawn from the trough between the 020-$1\bar{1}0$ peaks to the background immediately beyond the $11\bar{1}$ peak, by the height of $1\bar{1}0$ peak from the general background. XRD patterns were analyzed using the JADE 6.5 software.

188 **Fourier transform infrared spectroscopy (FT-IR)**

189 The FT-IR spectra were obtained on a Nicolet iS10 FT-IR spectrometer by using the
190 KBr pressed disk technique. The pressed disks were prepared by mixing samples and KBr at a
191 ratio of approximate 1:100, and ground in an agate mortar for homogenization. The mixture
192 was then heated under a lamp for 3 min to minimize water adsorption. The spectra were
193 collected over the range of 4000 - 400 cm^{-1} with 64 scans and a resolution of 4 cm^{-1}.

194

195 **Specific surface area (SSA), porosity and pore size distribution analysis**

196 Specific surface area (SSA) of representative samples were obtained via the nitrogen
197 adsorption (the BET method) using a Beckman Coulter SA3100 analyzer. All samples were
198 outgassed for 6 - 12 h and heated to a maximum temperature of 50°C to remove surface
199 moisture before the analysis. Porosity and pore size distribution of these samples was further
200 evaluated through the Barrett–Joyner–Halenda (BJH) method (Barrett et al., 1951).

201

202 **Cation Exchange Capability (CEC) characterization**

203 Cation Exchange Capability (CEC) characterization for the <2 μm and 2 - 20 fractions
204 was carried out following Deng et al. (2014). Samples were first treated with dilute acetic acid
205 to remove any possible carbonates and then washed by 0.5 M and 0.005 M $CaCl_2$ for 3 times
206 each to completely saturate the cation exchangeable sites and determine the volume of
207 interstitial solution. Ca-saturated samples were then washed with 0.5 M $MgCl_2$ for 4 times.

Supernatant solutions were collected after centrifugation and the Ca contents were analyzed with a PE Optima 8300 inductively coupled plasma-optical emission spectrometer (ICP-OES) at HKU.

Electron-probe micro-analysis (EPMA)

The major element contents of the kaolinite group minerals in soils and primary muscovite and feldspars were analyzed using a JEOL JXA-8230 electron microprobe at the Department of Earth Sciences, HKU. The analyses were performed using a 15 kV accelerating voltage and a 20 nA beam current. The beam spot diameter was varied from 1 to 5 μm to eliminate sample damage. The Kα line was chosen for all analyzed elements. Analytical conditions and applied standards are listed in Supplementary Table 1. All data were corrected using the standard ZAF correction procedures.

Clay-adsorbed REE concentration

Extraction experiment was conducted to quantify for the variations in adsorbed REE concentrations of the clay fractions from different soil horizons. The adsorbed REE portion here is operationally defined as easily extractable fraction by dilute electrolyte solutions. All centrifuge tubes and containers used were soaked in 1 M HNO_3 for over 24 h and rinsed repeatedly with Milli-Q double de-ionized water (Ω = 18.2M) before use. Ten ml of 0.5 M ammonium sulfate was added to 50 mg of clay separates and mechanically shaken for 16 hours

at room temperature to extract the REEs. The extracted solutions were collected by centrifuging at 10,000 rpm for 30 min and filtration using a cellulose acetate-type membrane filter (φ = 0.22μm). Residues after extraction were dried overnight at 40ºC and completely digested in a concentrated mixture of HF-HCl-HNO_3 at a temperature of ~180ºC. Acidified and diluted solutions were analyzed with an Agilent 7900 inductively coupled plasma-mass spectrometer (ICP-MS) at HKU. Both the accuracy and precision are at <10% for all analyzed elements.

Results

Particle size distribution

Results of particle size distribution for 26 samples are divided into ranges of <2, 2 - 20, 20 - 50, and >50 μm fractions. Average results of each range are summarized in Table 1 and Figure 3. Generally, proportion of fine particles becomes progressively more abundant from the lower part to upper part of the soil profile. In the lower saprolite, about half of the soil particles (~40%) are larger than 50 μm. Whereas there are about 8 and 30% for the <2 and 2 - 20 μm fractions respectively, slightly lower than those in the upper saprolite (9 and 38% respectively). These two fractions comprise 12 and 48%, respectively, of the lower pedolith and the highest as 23 and 58%, respectively, of the humic layer and upper pedolith. In contrast, the proportion of particles with sizes of >50 μm dramatically drops to 28% in the upper saprolite, then further to 15 and 5% in the lower and upper pedolith, respectively.

248 **SEM and HRTEM observation**

249 From SEM and HRTEM observation, morphology and association of clay minerals are
250 directly observed. Halloysite is the major clay species in the saprolite, and is grouped into two
251 types on the basis of appearance. The first type is very short, stubby, narrow, and tubular
252 halloysite. The length varies from <100 to 500 nm. The short halloysite tubes occur as
253 aggregates on surface and in etch pits of weathered feldspar grains (Fig. 4a). These halloysite
254 tubes are also commonly found along edges and cleavages of muscovite flakes (Fig. 4b & c),
255 either as aggregates or as individual tubes. The second type of halloysite is long tubular. These
256 halloysite tubes range from 1 to 5 μm in length and occur as aggregates on the surface of
257 weathered feldspar grains (Fig. 4d) through coalescence of short halloysite tubes (Fig. 4e).
258 Occasionally, the long halloysite tubes occur on the surface of weathered muscovite grains (Fig.
259 4f). Under HRTEM, d spacing of both 10Å (Fig. 4g) and 7Å (Fig. 4h) could be observed for
260 the halloysite tubes with open-ended cylindrical lumen pores of 10 - 20 nm across (Fig. 5).
261 However, the possibility of rapid dehydration of halloysite-10Å to the 7Å-species during
262 analysis cannot be ruled out. It is notable that the short halloysite tubes are closely associated
263 with muscovite (Fig. 5). Both close tubes with clear lumen pores (Fig. 5a, b & e) and semi-
264 open tubes (Fig. 5c - e) are abundant on the edges of the muscovite sheets. The semi-open tubes
265 may represent an interim stage of formation through rolling-up of the muscovite sheet. In
266 addition, the edges of the muscovite sheets are apparently thicker than the interior under TEM
267 imaging (Fig.5f), probably indicating thickening of sheets at margins due to rolling-up along

268 edges. Apart from halloysite, sub-ordinate amounts of kaolinite and illite also occur in the
269 saprolite. Kaolinite appears as irregular microcrystalline flakes, a few μm across, growing
270 topotaxially on the surface, and occasionally along the edges of weathered muscovite grains
271 (Fig. 6a & b). Illite grains are mostly of 1 - 5 μm across with irregular shapes and undulating
272 surfaces. Illite mainly occurs as aggregates on the surface of the weathered feldspar grains (Fig.
273 6c). Residual muscovite grains are common and occur as stacks with sheets of different sizes
274 and shapes (Fig. 6d).

275 In the humic layer and upper pedolith, platy kaolinite crystals become progressively
276 more abundant and larger in size, of up to 10 μm across. Apparently, these kaolinite "booklets"
277 were formed through the coalescence of halloysite, either on the basal surfaces of the kaolinite
278 booklet (Fig. 7a - e) or along the edge (Fig. 7f). Continuous growth of kaolinite ultimately
279 forms large, euhedral, vermicular kaolinite booklets (Fig. 7g) with a d spacing of ~7.2Å and
280 unit cells of ~5.0Å along the *a* axis (Fig. 8a). These kaolinite booklets are commonly observed
281 in the shallow soils, whereas euhedral long halloysite tubes of >1 μm long are occasionally
282 associated with kaolinite (Fig. 7h, 8b - d). In addition, halloysite, with a d-spacing of ~8.0Å,
283 has been observed under HR-TEM (Fig. 8c), suggesting a progressive dehydration of
284 halloysite-10Å to the 7Å type (Fig. 8d).

285

286 **Modal proportion of clay minerals from XRD spectra**

From the XRD spectra, different clay minerals have been identified and their relative proportions were calculated based on the corresponding peak intensities and heights (Table 2). The entire results are provided in Supplementary Table 2.

In the saprolite and lower pedolith, the <2 μm clay fraction has a higher abundance of kaolinite of 55 - 70% and of ~25 - 35% halloysite. Muscovite/illite contents are comparatively low, ranging from 2 to 9% in the lower pedolith and upper saprolite (Table 2; Fig. 3 & 9). There are trace amounts of other clay minerals, including smectite, interstratified muscovite-illite/smectite, vermiculite, and interstratified muscovite-illite/vermiculite. The 2 - 20 μm fraction generally has higher abundance in muscovite/illite (up to 19%), but similar abundances in kaolinite (47 - 73%) and halloysite (21 - 44%) to the <2 μm fraction. In the uppermost humic layer and upper pedolith, the proportion of kaolinite further increases to 60 - 70% but that of halloysite significantly drops to <10% (Table 2; Fig. 3 & 9). Interstratified muscovite-illite/vermiculite becomes much more abundant, sharing ~15 - 20% (Table 2). Contents of muscovite/illite and vermiculite are also slightly higher and range from ~6 to 10% (Table 2). It is noticed that the 2 - 20 μm fraction has a slightly higher abundance in muscovite/illite and interstratified muscovite-illite/vermiculite, but slightly lower abundance in vermiculite than the <2 μm fraction. To summarize, contents of halloysite gradually decrease with progressive weathering with a dramatic drop from the lower to upper pedolith, whereas contents of kaolinite increase significantly from the lower to upper saprolite and remain consistent in the pedolith (Fig. 3). Crystallinity of kaolinite in the <2 μm fraction gradually rises with progressive

weathering, as indicated by increases in the Hinckley Index from 0.14 in the lower saprolite to 0.50 in the upper saprolite and further to 0.76 and 0.98 in the lower and upper pedolith respectively (Table 2). Generally, kaolinite from the 2 - 20 μm fraction has a higher crystallinity than the <2 μm fraction from the same soil horizon with a maximum of 1.83 in the shallowest humic layer and upper pedolith (Table 2).

FT-IR spectra

Twelve samples were analyzed by FT-IR and representative spectra are shown in Figure 10. Generally, spectra obtained from the <2 and 2 - 20 μm fractions are extraordinarily similar suggesting similar clay assemblages in both fractions. Halloysite could be differentiated from kaolinite in FT-IR spectra by exhibiting only two Al_2OH-stretching bands at approximately 3695 and 3620 cm^{-1} and a sharp single Al_2OH-bending band at ~920 cm^{-1} without shoulders. Whereas well-developed Al_2OH-stretching bands at ~3695, 3670, 3650, and 3620 cm^{-1} and a broad shoulder at ~940 cm^{-1} associated with the Al_2OH-bending band could be observed for well-crystallized kaolinite. Hence, clay minerals are dominated by halloysite in the lower saprolite. A broad stretching band for the Si-O bond developed at ~1040 cm^{-1} with a poorly developed shoulder at ~1100 cm^{-1} further implies low crystallinity. The proportion of kaolinite progressively increases in the upper saprolite and lower pedolith, as evident by the appearance of weak Al_2OH-stretching bands at ~3670 and 3650 cm^{-1} and a narrow shoulder at ~940 cm^{-1}. Moreover, the kaolinite-group minerals become more crystalline as indicated by sharper SiO-

stretching bands at ~1010 and 1035 cm^{-1} and more developed SiO-stretching band at 1100 cm^{-1}. In the humic layer and upper pedolith, appearance of four sharp Al_2OH-stretching bands and a broad shoulder of the Al_2OH-bending band shows the dominance of crystalline kaolinite. High crystallinity of the clay minerals can also be interpreted by the well-developed SiO-stretching bands at ~1010 and 1035 cm^{-1} in the spectra.

Specific surface area, pore volume and pore size distribution

The specific surface area of 11 samples from different soil horizons were measured using the BET method (S_{BET}), and the BJH method for their pore volume and pore size distribution. The averaged results for each fraction are listed in Table 3. The entire results could be obtained in Supplementary Table 3. In the saprolite and lower pedolith, S_{BET} of the <2 and 2- 20 µm fractions vary from ~15 to 20 m^2/g and ~12 to 17 m^2/g, respectively. In the humic layer to upper pedolith, S_{BET} of both the <2 and 2 -20 µm fractions are comparatively much lower at ~8 and ~10 m^2/g, respectively (Fig. 3). From the adsorption and desorption isotherms shown in Figure 11a, only very little hysteresis is shown for all samples, and moreover, generally low values for the differences between the cumulative SSA from either the adsorption (S_{ads}) or desorption (S_{des}) isotherms and the S_{BET} (Table 3). This suggests that the dominant pore shape in all samples is cylindrical (Churchman et al., 1995; Pasbakhsh et al., 2013).

For the pore size, both the average BJH adsorption and desorption cumulative pore volumes of the <2 and 2 -20 µm fractions are consistently of 0.10 - 0.12 and 0.06 - 0.07 cm^3/g,

347 respectively, in the saprolite and lower pedolith, but decrease by half to 0.06 cm^3/g for the <2
348 µm fraction in the humic layer and upper pedolith (Table 3; Fig. 3). A bimodal distribution of
349 the pore size is observed for the clay minerals in all soil horizons (Fig. 11b). The clay minerals
350 from the saprolite and lower pedolith are dominated by fine micropores with a narrow
351 distribution of sizes of ~2 - 3 nm, which may be attributed to the internal and/ or surface pores
352 (Pasbakhsh et al., 2013). Mesopores with sizes of ~10 nm are sub-ordinately abundant (Fig.
353 10b) and contributed primarily from the central lumen pores of the halloysite tubes (Pasbakhsh
354 et al., 2013). In the humic layer and upper pedolith, the abundance of the micropore
355 dramatically decreases, whereas the ~10 nm mesopores rarely exist (Fig. 11b). Alternatively,
356 mesopores with a broad distribution of around 12 nm occur likely due to the abundance of
357 kaolinite (Pasbakhsh et al., 2013).
358
359 **Cation exchange capacity**
360 Eleven samples from different soil horizons have been measured for the CEC and the
361 averaged results are tabulated in Table 3. In general, CEC in different soil horizons vary slightly
362 (Fig. 3). The CEC from both the <2 and 2 - 20 µm clay fractions increases slightly from the
363 lower saprolite to the upper saprolite and lower pedolith, from 13 to ~15 and from 11 to ~14 c
364 mol/kg^{-1} on average, respectively. The CEC of the <2 µm fraction at the humic layer and upper
365 pedolith fundamentally remains the same, yet, that of the 2 - 20 µm fraction decreases to ~11
366 c mol/kg^{-1} on average (Fig. 3).

Chemical composition of minerals

Unweathered grains of muscovite and feldspars from the parent rock and the kaolinite group minerals from different soil horizons have been analyzed. Results are summarized in Tables 4 and 5 and the full dataset is available in Supplementary Table 4 - 6. Fresh muscovite has SiO_2, Al_2O_3, and K_2O contents of 45.3, 32.3, and 10.7 wt. % on average, respectively. Notably, muscovite is Fe-rich and contains up to ~8.5 wt. % of FeO. Feldspar of the primary granite is mainly of orthoclase and albite. Orthoclase has 63.1 wt. % SiO_2, 17.5 wt. % Al_2O_3, and 16.7 wt. % K_2O on average, whereas albite has 67.0 wt. % SiO_2, 18.9 wt. % Al_2O_3, and 11.7 wt. % Na_2O on average.

In the lower saprolite, the kaolinite group minerals have 44.9 wt. % SiO_2, 37.5 wt. % Al_2O_3, and 2.12 wt. % FeO on average, respectively. With progressive weathering, the SiO_2 and Al_2O_3 contents of the kaolinite group minerals subsequently increase to ~45 and 38 wt. % respectively in the upper saprolite and pedolith. Average FeO contents gradually decrease to 0.55 - 1.57 wt. % in the lower pedolith and upper saprolite, and to 0.46 wt. % in the humic layer and upper pedolith (Table 5). EPMA showed that Fe + Si is inversely proportional to Al in the kaolinite group minerals (Fig. 12a). Further supported by the scarce observation of Fe-rich particles associated with the kaolinite group minerals, coupled substitution between Fe + Si and Al should have accounted for the Fe content (Jige et al., 2018). Moreover, Fe in the kaolinite group minerals mainly occurs as the Fe^{3+} for Al^{3+} substitution, although minor Fe^{2+}

for Al^{3+} substitution takes place in some samples from the lower pedolith and saprolite (Fig. 12b).

Clay-adsorbed REE concentration

As the separation of the clay fractions were performed mechanically, it is inevitable that sub-µm sized supergene REE minerals, such as chernovite-(Y) (Li et al., 2019), and residual REE minerals were also extracted as well. In this regard, the extracted clay fractions were treated with ammonium sulfate extraction instead of bulk analysis to estimate the REE concentrations that are weakly bound to the clay minerals, likely through adsorption. Nonetheless, the residues after extraction were analyzed for comparison. The results are summarized in Table 6 and fully tabulated in Supplementary Table 7. The variation of clay-adsorbed REE concentrations generally follows that of the bulk soils (Fig. 13). Clay fractions from the lower pedolith and upper saprolite have the highest adsorbed REE concentrations, of ~3,500 and 2,500 ppm respectively (Table 6). The concentrations are comparatively lower in the lower saprolite (~1,000 ppm in average for both fractions). Notably, the clay-adsorbed concentrations of the <2 and 2 - 20 µm fractions are largely comparable in the lower pedolith and saprolite (Fig. 3). Whereas, the adsorbed REE concentrations of the 2 - 20 µm fractions are significantly lower than the corresponding <2 µm fractions in the humic layer and upper pedolith and only of ~70 ppm, comparing to >200 to ~1,200 ppm in the <2 µm fractions (Table 6; Fig. 3). In general, the $(La/Yb)_N$ values of the clay fractions from all soil horizons are similar

(Table 6), with those from the humic layer and pedolith are slightly higher, indicating a slight enrichment of the LREEs. In contrast, Ce anomaly varies significantly. Clay fractions from the lower pedolith and saprolite exhibit significantly negative Ce anomalies of 0.02 to 0.08, yet, Ce anomalies in the humic layer and upper pedolith have become less negative of 0.8 on average for the <2 μm fractions, and even become positive of 1.7 on average for the 2 - 20 μm fractions (Table 6; Fig. 13). In the lower pedolith and saprolite, REE concentrations of the residues (including Fe-Mn oxyhydroxide-sorbed, organic substance-bound, and crystalline phase-hosted REEs) after extraction are generally of one-third of the clay-adsorbed concentrations (Table 6; Fig. 3). This proves that most of the REEs in the clay fractions occur in weakly adsorbed state. However, in humic layer and upper pedolith, the REE concentrations in the clay fractions could be of higher for the residual portion than the clay-adsorbed portion, especially in the 2 – 20 μm fraction (Table 6; Fig. 3). This illustrates a less important role in adsorption on clay minerals in the shallow soils. The comparatively high As concentrations in the residues of the clay fractions from the lower pedolith and saprolite implies that significant amount of the residual REEs are likely hosted in supergene chernovite-(Y), in consistent with previous observation (Li et al., 2019).

Discussions

Transformation of clay minerals in progressive weathering

From the previous results, the following major mineralogical transformation pathways are proposed to have occurred at the Zudong deposit with progressive weathering, causing the variations in their abundance (Fig. 1a):

1. Muscovite → Short, tubular halloysite-10Å → Halloysite-7Å (either short or long and tubular) → Vermicular kaolinite
2. Muscovite → Microcrystalline kaolinite → Vermicular kaolinite
3. Muscovite → Illite, Illite/Smectite & Illite/Vermiculite → Vermiculite
   (Subordinate importance and more restricted to the shallow soils)
4. Feldspar → Halloysite (either short or long and tubular) → Vermicular kaolinite
5. Feldspar → Illite → Kaolinite

In the lower saprolite, representing an incipient stage of weathering, weathering of muscovite formed short halloysite tubes and subordinately, microcrystalline kaolinite in the saprolite. From SEM and HRTEM observation, it is evident that muscovite gradually transformed to halloysite through rolling-up of the edges (Fig. 5). As primary muscovite was formed through metasomatism of biotite (Huang et al., 1989), the comparatively high concentration of Fe inherited in the muscovite (Table 5) would probably induce higher lattice strain and motivate the decomposition of muscovite. During weathering, it is postulated that the interlayer K cation and a tetrahedral sheet of muscovite would be preferentially removed while a T-O sheet remained. Under a water saturated environment, misfit between the octahedral and tetrahedral sheets were compensated for by rolling and incorporation of

446 interlayer water molecules to form halloysite-10Å (Bailey, 1990; Singh, 1996). On the other
447 hand, aggregates of short halloysite tubes along edges of muscovite sheets (Fig. 4b) suggest an
448 alternative dissolution-precipitation mechanism for the growth of halloysite, during which
449 dissolution of muscovite led to local supersaturation of Si and Al in the soil solutions that
450 motivated the rapid precipitation of halloysite nano-tubes (Lu et al., 2016). Whereas
451 microcrystalline kaolinite mostly appears to form topotaxially on muscovite, especially along
452 cleavages (Aoudjit et al., 1996; Robertson and Eggleton, 1991; Singh and Gilkes, 1991).

453 Feldspar can be decomposed to form halloysite and illite during the incipient
454 weathering (Eswaran and Bin, 1978; Inoue et al., 2012; Jeong, 1998a; Papoulis et al., 2004).
455 Albite can decompose more rapidly than orthoclase during weathering (Banfield and Eggleton,
456 1990; Blum and Stillings, 1995; White et al., 2001). During dissolution of albite, Na and Ca
457 were lost to the soil solutions, whereas local oversaturation of Si and Al provoked the
458 simultaneous crystallization of halloysite-10Å under a water saturated condition (Banfield and
459 Eggleton, 1990; Velde, 1985). Such a rapid precipitation is demonstrated by meshes of short
460 halloysite tubes and in etch pits on the surface of the albite grains (Fig. 4a). Subsequently, these
461 halloysite nanotubes would coalescence and transform into more stable long halloysite tubes
462 (Fig. 4e). Weathering of orthoclase formed illite during incipient weathering (Fig. 6c) due to
463 local equilibria at grain contacts between orthoclase and muscovite, providing sufficient K
464 during mineral decomposition to precipitate illite (Meunier and Velde, 1976). Rapid formation
465 of halloysite and microcrystalline kaolinite of low crystallinity prevailed during incipient

466 weathering. With progressive weathering, the short, stubby halloysite coalesced to form long,
467 tubular halloysite and kaolinite in the lower pedolith and upper saprolite.

468 In the upper pedolith, which represents a more advanced stage of weathering, soils
469 would be subjected to repeated wetting and drying episodes, causing irreversible dehydration
470 of metastable halloysite-10Å to halloysite-7Å and further transformation to kaolinite
471 (Churchman and Carr, 1975; Inoue et al., 2012; Jeong, 1998a; Jeong, 1998b; Papoulis et al.,
472 2004; Singer et al., 2004; Wouatong et al., 1996). The dehydration process is exemplified by
473 the occurrence of halloysite with a d spacing of ~8.0Å (Fig. 8c), which indicates dehydration
474 and shrinking of halloysite-10Å (Churchman et al., 1972; Giese, 1988). Also, crystalline,
475 vermicular kaolinite became progressively dominant towards shallow soils (Table 3; Fig. 7).
476 Evidently, these kaolinite "booklets" have grown through continuous coalescence of halloysite
477 along edges (Fig. 7a - e) and at basal sites (Fig. 7f) of kaolinite grains. During this
478 transformation, kaolinite grains of sizes up to 10 μm could have high crystallinity, as shown in
479 the FT-IR spectra (Fig. 10), and comparatively low Fe contents (<0.5 wt. % in average) (Table
480 5). Here, we postulate the halloysite-kaolinite transformation can be achieved through a solid-
481 state alteration after prolonged dehydration (Churchman and Gilkes, 1989). Unrolling of the
482 halloysite tubes can be possible after prolonged dehydration (Wouatong et al., 1996), as
483 removal of the interlayer water molecules could make tetrahedral rotation feasible to
484 accommodate the misfit between the octahedral and tetrahedral sheets in platy kaolinite (Bailey,
485 1990; Radoslovich, 1963; Singh, 1996). Alternatively, long-tubed halloysite (Fig. 7h & 8b) and

crystalline kaolinite could have also grown epitaxially to form aggregates, precipitated from the soil solutions (Banfield and Eggleton, 1990; Singh and Gilkes, 1991). Restricted occurrence of interstratified muscovite-illite/vermiculite and vermiculite in this part (Table 2; Fig. 9) suggests an alternative transformation pathway in more oxidizing shallow soils.

Physicochemical variation of clay minerals in progressive weathering

Transformation of clay minerals in progressive weathering could cause significant changes in physicochemical properties of the clay assemblages, such as the SSA and the CEC (e.g. Bobos et al., 2001; Papoulis et al., 2004). In the saprolite and lower pedolith, the kaolinite group minerals have comparatively high CEC and SSA (Table 3; Fig. 3). High abundance of short, stubby halloysite and microcrystalline kaolinite with high CEC could have strong edge and surface effects for adsorption (Hart et al., 2002; Ma and Eggleton, 1999; Singh and Gilkes, 1992). Likewise, low crystallinity, as indicated by the Hinckley Index (Table 2) and high Fe contents (Table 5), also contributes to the high CEC (Hart et al., 2003; Wilson et al., 2013). Substitution of Fe for Al in clay minerals can cause permanent negative charge either through substitution of Fe^{2+} for Al^{3+} in the octahedral sheet (Singh and Gilkes, 1992; Tazaki, 1981) or non-stoichiometric Fe^{3+} for Al^{3+} substitution (Soma et al., 1992). In the soil profile, Fe^{3+} for Al^{3+} substitution dominates, yet Fe^{2+} for Al^{3+} substitution also occurs especially in the lower saprolite (Fig. 12). Moreover, a large contribution to the CEC also comes from pH-dependent defect sites, such as broken bonds at edge and on basal surfaces, due to lattice deformation and

506 dislocation, mainly attributed to the Fe for Al substitution and the poor crystalline nature. Clay
507 minerals in these layers are also of high SSA and large pore volume compared to the shallow
508 soils (Table 3; Fig. 11). Specifically, the high SSA could be due to the abundant nano-sized
509 tubular halloysite and fine-grained poorly crystallized kaolinite (Wilson et al., 2013). Both the
510 central lumen and the fine internal and/ or surface pores of the tubular halloysite contribute to
511 the large pore volumes, especially the fine pores as revealed by the non-hysteretic feature in
512 the nitrogen adsorption and desorption isotherms (Fig. 11a) (Churchman et al., 1995). Small
513 aggregates of kaolinite, which frequently occur in these soil layers (Fig. 6a and b), also have
514 significantly higher porosity than large aggregates (Jozefaciuk, 2009).

515 In the shallow upper pedolith, transformation of tubular halloysite and microcrystalline
516 kaolinite to large, euhedral, vermicular kaolinite is associated with dramatic drops in the SSA
517 and porosity of the clay minerals (Table 3; Fig. 3). During the transformation, the growth in
518 crystalline kaolinite, as indicated by the increase of the Hinckley Index (Table 2) and associated
519 with a decrease in the Fe content (Table 5), significantly eliminated the amount of both
520 permanently and variably charged sites. Moreover, growth in size also causes a drop in the
521 CEC (Joussein et al., 2005). Although the CEC of the clay assemblages only varies slightly
522 from the lower to the upper pedolith (Table 3), this is attributed to the abundance of
523 interstratified muscovite-illite/vermiculite and vermiculite in the humic layer and upper
524 pedolith (Table 2). 2:1 layer clay minerals, such as illite and vermiculite, would generally have
525 a large CEC due to the permanent negative charge in their structures (Joussein et al., 2005;

Wilson et al., 2013). Compared to the CEC, the SSA and porosity of the clay minerals dramatically drops (Table 3; Fig. 3 & 11). This is mainly because of the conversion of halloysite to kaolinite. During this transformation, it is postulated that tubular halloysite unrolled to form platy kaolinite (Wouatong et al., 1996), resulting in a significant reduction in surface area and subsequent reduction in the amount of lumen pores. Coalescence of microcrystalline kaolinite to form large aggregates of vermicular kaolinite have also caused a decrease in the SSA and in the porosity (Jozefaciuk, 2009).

Relation between clay minerals and HREE accumulation

The physicochemical variations of the clay minerals, due to progressive weathering, highlight the contrasting adsorption capacities of the clay minerals from different soil horizons and explain the trends in mineralogy and geochemistry of the deposit. In a previous study (Li et al., 2019), bulk REE contents in the soils are documented to increase with depth from the humic layer and upper pedolith and to reach their maximum in the lower pedolith and upper saprolite (Table 1; Fig. 13b). The proportion of extractable REEs also follows a similar trend, increasing from ~45% in the shallow soils to 60 - 65% in the ore-bearing lower pedolith and upper saprolite (Table 1; Fig. 13b) (Li et al., 2019). The same trend has been observed for the clay fractions (Fig. 3 & 13a). The extraction experiment of the clay fractions performed in this study have further proved that the fine-grained portions control the REE enrichment in these deposits (Wu et al., 1990). Variations for both bulk and clay-adsorbed REE concentrations are

546 due to the much higher adsorption capacity of the clay minerals in the lower part than the upper
547 part of the soil profile. High CEC, large SSA, and high porosity of the small, poorly crystalline
548 halloysite and kaolinite in the lower part of soil profile are critical to facilitate REE adsorption.
549 In addition, it is likely that halloysite contributes more greatly to the REE adsorption and
550 enrichment (Fig. 14). The proportion of halloysite in the clay fractions are positively correlated
551 with both the adsorbed HREEs (Fig. 14a) and LREEs (Fig. 14b) concentrations, especially for
552 the saprolite, although it is probable that kaolinite also plays an important role in adsorbing the
553 REEs in the lower pedolith. Whereas, no obvious correlation between the proportion of
554 kaolinite and either HREEs (Fig. 14c) or LREEs (Fig. 14d) is exhibited. Although the mode of
555 REE adsorption is still not well understood, it is possible that the HREEs could be adsorbed in
556 the interlayer position of halloysite. Abundant halloysite in the lower part of the soil profile
557 would greatly facilitate adsorption under this mechanism. Another recent study proposed that
558 the REEs are adsorbed as 9 - 10 coordinated hydrated outer sphere complexes on the basal sites
559 of kaolinite (Borst et al., 2018). Therefore, it is likely that the REEs, especially the LREEs,
560 could be partially adsorbed as hydrated complexes in the central lumen pores of the tubular
561 halloysite and basal surfaces of the microcrystalline kaolinite in this scenario.

562 In the upper part of the soil profile, the adsorption capacity of the clay minerals
563 dramatically decreases along with drops in the CEC, SSA, and porosity during the
564 transformation of halloysite and microcrystalline kaolinite to crystalline kaolinite. This induces
565 REE desorption, which results in a lower proportion of adsorbed REEs (Table 6; Fig. 13a),

566 although the contents of fine particles and the kaolinite group minerals (Table 1) are higher in
567 the shallow soils (Li et al., 2019). In addition to the decreases in the SSA and porosity (Table
568 3; Fig. 11), unrolling of the tubular halloysite would expose the adsorbed REEs located in the
569 internal and lumen pores directly to the soil solutions, making desorption much more feasible.
570 Consequently, the clay-adsorbed and bulk REE concentrations dramatically decrease in the
571 humic layer and upper pedolith (Table 1 & 6; Fig. 13 & 15). Considering that the potential of
572 zero charge of kaolinite is generally below the pH of 4.5 (Kosmulski, 2018), kaolinite in the
573 shallow soils remain negatively charged (averaged soil pH of the humic layer and upper
574 pedolith = 4.74; Table 1). This suggests that part of the desorbed REEs would be re-adsorbed,
575 particularly for the <2 μm fraction (Table 6; Fig. 15). Alternatively, the relatively high clay-
576 adsorbed REE concentrations for the <2 μm fraction from the upper pedolith (Fig. 3 & 15a)
577 may suggest preferential REE desorption first on the larger-sized fractions, in consistent with
578 the sub-μm sized halloysite and kaolinite to larger-sized kaolinite transformation. This also
579 explains the much lower clay-adsorbed REE concentrations in the 2 – 20 μm fraction from the
580 humic layer and upper pedolith, compared to the residual REE concentrations (Table 6). The
581 desorbed REEs would be released into the soil solutions and transported downwards to deeper
582 parts of the soil profile, at where the clay minerals, comprising tubular halloysite and
583 microcrystalline kaolinite, have higher CEC, larger SSA, and higher porosity favoring the REE
584 adsorption. With time, continuous input of the REEs from shallow soils, and efficient

adsorption in the lower part of the soil profiles, would result in REE enrichment and ore formation (Li et al., 2019).

Implications

Here, we present a comprehensive study on the variation and transformation of clay minerals during progressive weathering of granite and the corresponding changes in different physicochemical properties that could significantly affect the REE adsorption and accumulation necessary to form world class regolith-hosted HREE deposits. Clay mineralogy is demonstrated to be a key factor in REE accumulation during weathering. Transformation of metastable halloysite and microcrystalline kaolinite to euhedral, crystalline kaolinite in the shallow soils, during which the CEC, SSA and porosity could dramatically decrease, is critical for REE desorption in the shallow soils. Whereas preservation of poorly crystallized halloysite and kaolinite in the deep regolith significantly facilitated the REE adsorption there. Through time, continuous operation of such an eluviation - illuviation process could result in sufficient REE accumulation to form economically valuable deposits.

Hence, several implications could be drawn for resources exploration and metallurgical practice. Contrasting variations in physicochemical properties of kaolinite group minerals along soil profiles could be a promising exploration tool for regolith-hosted HREE resources. Preservation of halloysite in the lower part of the soil profile, coupled with its destruction in the upper part of the same soil profile could be a good indicator for REE enrichment in the

lower soil horizons. As the REEs are largely adsorbed on halloysite, most likely preferentially in the internal and lumen pores, the properties of halloysite should be taken into consideration for exploration and metallurgical processing. Halloysite could form intercalated complexes with certain salts, such as K-acetate, KCl, NH_4Cl, $(NH_4)_2SO_4$, RbCl, and CsCl (Carr et al., 1978; Wada, 1959a; Wada, 1959b). This is partially why ammonium sulfate is a very efficient leaching agent for industrial extraction of the REEs from these deposits. Compounds that could form stable intercalated complexes with halloysite would be of interest in the future design of more environmental friendly metallurgical processes.

Acknowledgements

We would like to thank the kind assistance of Xiao Fu for EPMA, Lily Chiu for PSA, Maria Lo for ICP-OES analysis, and Frankie Chan from the EMU for TEM analysis. Youjun Deng from the Texas A&M University is acknowledged for the kind provision of his soil mineralogy laboratory manual. Daniel E. Harlov is thanked for his constructive comments and language polishing on the manuscript. Editorial handling by Editor Hongwu Xu, Associate Editor Andy Madden, and constructive comments by Kenzo Sanematsu and an anonymous reviewer are gratified. This study was supported financially by a Seed Fund from HKU (201611159130) to M.-F.Z.

References

625 Aoudjit, H., Elsass, F., Robert, M., and Righi, D. (1996) Mica weathering in acidic soils by analytical
626 electron microscopy. Clay Minerals, 31(3), 319-332.
627 Bailey, S.W. (1990) Halloysite-A critical assessment. Sciences Géologiques, bulletins et mémoires,
628 86(1), 89-98.
629 Banfield, J.F., and Eggleton, R.A. (1990) Analytical transmission electron microscope studies of
630 plagioclase, muscovite, and K-feldspar weathering. Clays and Clay Minerals, 38(1), 77-89.
631 Bao, Z., and Zhao, Z. (2008) Geochemistry of mineralization with exchangeable REY in the weathering
632 crusts of granitic rocks in South China. Ore Geology Reviews, 33(3), 519-535.
633 Barrett, E.P., Joyner, L.G., and Halenda, P.P. (1951) The determination of pore volume and area
634 distributions in porous substances. I. Computations from nitrogen isotherms. Journal of the
635 American Chemical society, 73(1), 373-380.
636 Berger, A., Janots, E., Gnos, E., Frei, R., and Bernier, F. (2014) Rare earth element mineralogy and
637 geochemistry in a laterite profile from Madagascar. Applied geochemistry, 41, 218-228.
638 Blum, A.E., and Stillings, L.L. (1995) Feldspar dissolution kinetics. Reviews in Mineralogy and
639 Geochemistry, 31(1), 291-351.
640 Bobos, I., Duplay, J., Rocha, J., and Gomes, C. (2001) Kaolinite to halloysite-7 Å transformation in the
641 kaolin deposit of São Vicente de Pereira, Portugal. Clays and Clay Minerals, 49(6), 596-607.
642 Borst, A.M., Smith, M.P., Finch, A., Marquis, E., Estrade, G., Kynicky, J., Xu, C., and Geraki, K. (2018)
643 Structural state of REE in ion adsorption deposits: A XANES/EXAFS study of laterites from
644 Madagascar and China. Proceedings of the Resources for Future Generations Conference,
645 Vancouver.

646 Carr, R., Chaikum, N., and Patterson, N. (1978) Intercalation of salts in halloysite. Clays and Clay
647 Minerals, 26(2), 144-152.
648 Cheshire, M.C. (2011) Isotopic and geochemical composition of the Georgia kaolins: Insights into
649 formation and diagenetic conditions, PhD, p. 244. Indiana University.
650 Cheshire, M.C., Bish, D.L., Cahill, J.F., Kertesz, V., and Stack, A.G. (2018) Geochemical Evidence for
651 Rare-Earth Element Mobilization during Kaolin Diagenesis. ACS Earth and Space Chemistry,
652 2(5), 506-520.
653 Churchman, G., Aldridge, L., and Carr, R. (1972) The relationship between the hydrated and dehydrated
654 states of an halloysite. Clays and Clay Minerals, 20(4), 241-246.
655 Churchman, G., and Carr, R. (1975) The definition and nomenclature of halloysites. Clays and Clay
656 Minerals, 23(5), 382-388.
657 Churchman, G., Davy, T., Aylmore, L., Gilkes, R., and Self, P. (1995) Characteristics of fine pores in
658 some halloysites. Clay Minerals, 30(2), 89-98.
659 Churchman, G., and Gilkes, R. (1989) Recognition of intermediates in the possible transformation of
660 halloysite to kaolinite in weathering profiles. Clay Minerals, 24(4), 579-590.
661 Deng, Y., White, G.N., and Dixon, J.B. (2014) Soil mineralogy laboratory manual. 201 p. Department
662 of Soil and Crop Sciences. Texas A &M University, College Station, US.
663 Elliott, W.C., Gardner, D.J., Malla, P., and Riley, E. (2018) A New Look at the Occurrences of the
664 Rare-Earth Elements in the Georgia Kaolins. Clays and Clay Minerals, 66(3), 245-260.
665 Eswaran, H., and Bin, W.C. (1978) A study of a deep weathering profile on granite in peninsular
666 Malaysia: II. Mineralogy of the clay, silt, and sand fractions. Soil Science Society of America
667 Journal, 42(1), 149-153.

668 Giese, R. (1988) Kaolin minerals; structures and stabilities. Reviews in Mineralogy and Geochemistry,
669 19(1), 29-66.
670 Hart, R., Wiriyakitnateekul, W., and Gilkes, R. (2003) Properties of soil kaolins from Thailand. Clay
671 Minerals, 38(1), 71-94.
672 Hart, R.D., Gilkes, R.J., Siradz, S., and Singh, B. (2002) The nature of soil kaolins from Indonesia and
673 Western Australia. Clays and Clay Minerals, 50(2), 198-207.
674 Hinckley, D.N. (1962) Variability in "crystallinity" values among the kaolin deposits of the coastal
675 plain of Georgia and South Carolina. Clays and clay minerals, 11(1), 229-235.
676 Huang, D., Wu, C., and Han, J. (1989) REE geochemistry and mineralization characteristics of the
677 Zudong and Guanxi granites, Jiangxi Province. Acta Geologica Sinica (English edition), 2(2),
678 139-157.
679 Huang, J., Sun, S., and Zhang, J. (2013) Detection of trends in precipitation during 1960–2008 in Jiangxi
680 province, southeast China. Theoretical and applied climatology, 114(1-2), 237-251.
681 Inoue, A., Utada, M., and Hatta, T. (2012) Halloysite-to-kaolinite transformation by dissolution and
682 recrystallization during weathering of crystalline rocks. Clay Minerals, 47(3), 373-390.
683 Jeong, G.Y. (1998a) Formation of vermicular kaolinite from halloysite aggregates in the weathering of
684 plagioclase. Clays and Clay Minerals, 46(3), 270-279.
685 -. (1998b) Vermicular kaolinite epitactic on primary phyllosilicates in the weathering profiles of
686 anorthosite. Clays and Clay Minerals, 46(5), 509-520.
687 Jige, M., Takagi, T., Takahashi, Y., Kurisu, M., Tsunazawa, Y., Morimoto, K., Hoshino, M., and
688 Tsukimura, K. (2018) Fe-kaolinite in granite saprolite beneath sedimentary kaolin deposits: A

689 mode of Fe substitution for Al in kaolinite. American Mineralogist: Journal of Earth and
690 Planetary Materials, 103(7), 1126-1135.
691 Joussein, E., Petit, S., Churchman, J., Theng, B., Righi, D., and Delvaux, B. (2005) Halloysite clay
692 minerals–a review. Clay Minerals, 40(4), 383-426.
693 Jozefaciuk, G. (2009) Effect of the size of aggregates on pore characteristics of minerals measured by
694 mercury intrusion and water-vapor desorption techniques. Clays and Clay Minerals, 57(5), 586-
695 601.
696 Kosmulski, M. (2018) The pH dependent surface charging and points of zero charge. VII. Update.
697 Advances in colloid and interface science, 251, 115-138.
698 Li, M.Y.H., Zhou, M.-F., and Williams-Jones, A.E. (2019) The genesis of regolith-hosted heavy rare
699 earth element deposits: Insights from the world-class Zudong deposit in Jiangxi Province, South
700 China. Economic Geology, 114(3), 541-568.
701 Li, Y.H.M., Zhao, W.W., and Zhou, M.-F. (2017) Nature of parent rocks, mineralization styles and ore
702 genesis of regolith-hosted REE deposits in South China: An integrated genetic model. Journal
703 of Asian Earth Sciences, 148, 65-95.
704 Liu, X., Chen, Y., Wang, D., Huang, F., and Zhao, Z. (2016) The metallogenic geomorphic condition
705 analysis of the ion-adsorbing type rare earth ore in the eastern Nanling region based on DEM
706 data. Acta Geoscientica Sinica, 37(2), 174-184 (in Chinese with English abstract).
707 Lu, Y., Wang, R., Lu, X., Li, J., and Wang, T. (2016) Reprint of Genesis of halloysite from the
708 weathering of muscovite: Insights from microscopic observations of a weathered granite in the
709 Gaoling Area, Jingdezhen, China. Applied Clay Science, 119, 59-66.

710 Ma, C., and Eggleton, R.A. (1999) Cation exchange capacity of kaolinite. Clays and Clay minerals,
711 47(2), 174-180.
712 Meunier, A., and Velde, B. (1976) Mineral reactions at grain contacts in early stages of granite
713 weathering. Clay Minerals, 11(3), 235-240.
714 Miller, W., and Keller, W. (1963) Differentiation between endellite-halloysite and kaolinite by
715 treatment with potassium acetate and ethylene glycol. Clays and Clay Minerals, 10, 244-253.
716 Moldoveanu, G., and Papangelakis, V. (2016) An overview of rare-earth recovery by ion-exchange
717 leaching from ion-adsorption clays of various origins. Mineralogical Magazine, 80(1), 63-76.
718 Padrones, J.T., Imai, A., and Takahashi, R. (2017) Geochemical behavior of rare earth elements in
719 weathered granitic rocks in northern Palawan, Philippines. Resource Geology, 67(3), 231-253.
720 Papoulis, D., Tsolis-Katagas, P., and Katagas, C. (2004) Progressive stages in the formation of kaolin
721 minerals of different morphologies in the weathering of plagioclase. Clays and Clay Minerals,
722 52(3), 275-286.
723 Pasbakhsh, P., Churchman, G.J., and Keeling, J.L. (2013) Characterisation of properties of various
724 halloysites relevant to their use as nanotubes and microfibre fillers. Applied Clay Science, 74,
725 47-57.
726 Radoslovich, E. (1963) The cell dimensions and symmetry of layer-lattice silicates. VI. Serpentine and
727 kaolin morphology. American Mineralogist: Journal of Earth and Planetary Materials, 48(3-4),
728 368-378.
729 Robertson, I.D., and Eggleton, R.A. (1991) Weathering of granitic muscovite to kaolinite and halloysite
730 and of plagioclase-derived kaolinite to halloysite. Clays and Clay Minerals, 39(2), 113-126.

731 Rudnick, R.L., and Gao, S. (2003) Composition of the continental crust. Treatise on geochemistry, 3,
732 659.
733 Sanematsu, K., Kon, Y., and Imai, A. (2015) Influence of phosphate on mobility and adsorption of
734 REEs during weathering of granites in Thailand. Journal of Asian Earth Sciences, 111, 14-30.
735 Sanematsu, K., Kon, Y., Imai, A., Watanabe, K., and Watanabe, Y. (2013) Geochemical and
736 mineralogical characteristics of ion-adsorption type REE mineralization in Phuket, Thailand.
737 Mineralium Deposita, 48(4), 437-451.
738 Sanematsu, K., and Watanabe, Y. (2016) Characteristics and genesis of ion-adsorption type deposits.
739 Reviews in Economic Geology, 18, 55-79.
740 Simandl, G. (2014) Geology and market-dependent significance of rare earth element resources.
741 Mineralium Deposita, 49(8), 889-904.
742 Singer, A., Zarei, M., Lange, F., and Stahr, K. (2004) Halloysite characteristics and formation in the
743 northern Golan Heights. Geoderma, 123(3-4), 279-295.
744 Singh, B. (1996) Why Does Halloysite Roll? - A New Model. Clays and Clay Minerals, 44(2), 191-196.
745 Singh, B., and Gilkes, R. (1991) Weathering of a chromian muscovite to kaolinite. Clays and Clay
746 Minerals, 39(6), 571-579.
747 -. (1992) An electron optical investigation of the alteration of kaolinite to halloysite. Clays and Clay
748 Minerals, 40(2), 212-229.
749 Soma, M., Churchman, G., and Iheng, B. (1992) X-ray photoelectron spectroscopic analysis of
750 halloysites with different composition and particle morphology. Clay Minerals, 27, 413-413.

751 Tazaki, K. (1981) Analytical electron microscopic studies of halloysite formation processesmorphology
752 and composition of halloysite. In M.M. Mortlan, and V.C. Farmer, Eds. Proceedings of the 6th
753 International Clay Conference 1978, p. 573-584. Elsevier.
754 Velde, B. (1985) Clay minerals: a physico-chemical explanation of their occurrence. Elsevier,
755 Amsterdam.
756 Wada, K. (1959a) An interlayer complex of halloysite with ammonium chloride. American
757 Mineralogist: Journal of Earth and Planetary Materials, 44(11-12), 1237-1247.
758 -. (1959b) Oriented penetration of ionic compounds between the silicate layers of halloysite. American
759 Mineralogist: Journal of Earth and Planetary Materials, 44(1-2), 153-165.
760 -. (1961) Lattice expansion of kaolin minerals by treatment with potassium acetate. American
761 Mineralogist: Journal of Earth and Planetary Materials, 46(1-2), 78-91.
762 White, A.F., Bullen, T.D., Schulz, M.S., Blum, A.E., Huntington, T.G., and Peters, N.E. (2001)
763 Differential rates of feldspar weathering in granitic regoliths. Geochimica et Cosmochimica
764 Acta, 65(6), 847-869.
765 Wilson, M., Deer, W., Howie, R., and Zussman, J. (2013) Rock-Forming Minerals, Volume 3C, Sheet
766 Silicates: Clay Minerals. Geological Society, London, p. 724.
767 Wouatong, A., Kitagawa, R., Takeno, S., Felix M, T., and Daniel, N. (1996) Morphological
768 transformation of kaolin minerals from granite saprolite in the western part of Cameroon. Clay
769 Science, 10(1), 67-81.
770 Wu, C., Huang, D., and Guo, Z. (1990) REE geochemistry in the weathered crust of granites, Longnan
771 area, Jiangxi Province. Acta Geologica Sinica (English Edition), 3, 193-209.

772 Xie, Y., Hou, Z., Goldfarb, R.J., Guo, X., and Wang, L. (2016) Rare earth element deposits in China.
773 Reviews in Economic Geology, 18, 115-136.
774 Yamaguchi, A., Honda, T., Tanaka, M., Tanaka, K., and Takahashi, Y. (2018) Discovery of ion-
775 adsorption type deposits of rare earth elements (REE) in Southwest Japan with speciation of
776 REE by extended X-ray absorption fine structure spectroscopy. Geochemical Journal, 52(5),
777 415-425.
778 Zhao, Z., Wang, D., Chen, Z., Chen, Z., Zhwng, G., and Liu, X. (2014) Zircon U-Pb age, endogenic
779 mineralization and petrogenesis of rare earth ore-bearing granite in Longnan, Jiangxi province.
780 Acta Geoscientica sinica, 35(6), 719-725.

781

782 **Figure Captions**

783 **Figure 1**. Simplified geological map of the Zudong deposit (after Li et al., 2019).

784

785 **Figure 2**. (a) A schematic soil profile and profile of REE content of the Zudong deposit (after
786 Li et al., 2019). (b - g) Field photos of the Zudong deposit. (b) Pedolith of orangish brown
787 appearance with abundant residual grains of quartz. (c) Interface between the pedolith and
788 saprolite at where the relict granitic texture progressively demolished. (d) Upper saprolite of
789 mottled pinkish white appearance due to the abundant kaolinized feldspar and relict granitic
790 texture is still preserved. (e) Lower saprolite of mottled purplish white appearance. (f) Saprock
791 in which outline of feldspar grains could still be preserved. (g) Fresh bedrock with major
792 minerals of quartz, orthoclase, and albite.

793

794 **Figure 3**. Variations of averaged particle size proportion, bulk mineral proportion and REE
795 distribution, and proportion of clay minerals, SSA, pore volume, CEC and clay-adsorbed REE
796 concentration of the clay fractions in different soil horizons. Abbreviations: Ab, albite; Gbs,
797 goethite; Hal, halloysite; Ill, illite; Kfs, K-feldspar; Kln, kaolinite; Ms, muscovite; Qtz, quartz;
798 Sme, smectite; Vrm, vermiculite. Ms-Ill/Sme and Ms-Ill/Vrm refer to interstratified muscovite-
799 illite with smectite and vermiculite respectively. Note that the proportion of kaolinite in the
800 bulk mineral proportion refers to the family of kaolinite group minerals. "1" indicates data
801 sourced from Li et al. (2019).

802

803 **Figure 4**. Occurrence of halloysite in the saprolite and lower pedolith. (a) - (f) are SEM images
804 while (g) and (h) are TEM images. Short, stubby halloysite tubes occur as (a) aggregates on
805 weathered albite and (b) muscovite or (c) as individual tubes on weathered muscovite. (d) Long
806 halloysite tubes occur as aggregates on weathered albite, (e) through coalescence of short
807 halloysite tubes and (f) on surface of weathered muscovite. Short, stubby halloysite tubes with
808 d spacing of (g) 10.1Å or (h) 7.5Å. Noted that the locations of d spacing measurement were
809 indicated by the red squares. Abbreviations: Ab, albite; Ms, muscovite.

810

811 **Figure 5**. Association of short halloysite tubes and muscovite at the saprolite and lower
812 pedolith. (a) - (d) are SEM images while (e) and (f) are TEM images. Nano-sized halloysite
813 with well grown tubular shapes and clear lumen pores (an example indicated by the black arrow
814 in e) are observed with *c* axes generally parallel to the muscovite sheet (examples indicated by
815 the blue arrows) and rolled up along edges of muscovite sheets form semi-open tubes
816 (examples indicated by the red arrows). Abbreviations: Ms, muscovite.

817

818 **Figure 6**. Occurrence of other clay minerals in the saprolite and lower pedolith. All images are
819 SEM images. (a) Microcrystalline kaolinite on weathered muscovite. (b) Aggregates of
820 microcrystalline kaolinite occasionally with long halloysite tubes. (c) Aggregates of illite on

821 surface of weathered orthoclase. (d) Weathered grain of muscovite occasionally with halloysite
822 tubes. Abbreviations: Hal, halloysite; Ill, illite; Kln, kaolinite; Ms, muscovite.
823
824 **Figure 7**. SEM images of the occurrence of clay minerals in the upper pedolith. (a) - (f)
825 Progressive transformation of halloysite to kaolinite. (a & b) The initial stage showing
826 coalescence of halloysite tubes along the edges to form sub μm-sized and loosely stacked
827 kaolinite. (c - f) The interim stage as vermicular kaolinite continues growing through
828 coalescence of the halloysite tubes along (d & e) edges and (f) basal surface. (g) Crystalline
829 vermicular kaolinite. (h) Aggregates of kaolinite and halloysite.
830
831 **Figure 8**. TEM images of the occurrence of clay minerals in the upper pedolith. (a) Crystalline
832 kaolinite with unit cells of 5.0Å along the *a* axis. (b) Long, tubular halloysite associated with
833 kaolinite with d spacing of (c) 8.0Å and (d) 7.4Å.
834
835 **Figure 9**. Representative XRD spectra of the clay fractions from different soil horizons.
836 Notations: N, Oriented samples; E, ethylene glycol-solvated samples; T, 550ºC heated samples;
837 K, K-acetate & ethylene glycol-solvated samples. Abbreviations: Ill, illite; Ms, muscovite; Vrm:
838 vermiculite.
839
840 **Figure 10**. Representative FT-IR spectra of the clay fractions from different soil horizons.
841

842 **Figure 11**. (a) Adsorption (represented by the solid line) and desorption (represented by the
843 dashed line) isotherms and (b) pore size distribution of the clay fractions in different soil
844 horizons.
845
846 **Figure 12**. Correlation plot between (a) (Si – 4) + Fe and Al, and (b) Fe and Al (VI) in kaolinite
847 group minerals from different soil horizons.
848
849 **Figure 13**. Upper continental crust (UCC)-normalized REE patterns of (a) the clay fractions
850 and (b) the bulk compositions from different soil horizons. Solid and dash lines in (a) represent
851 <2 and 2 - 20 μm fractions respectively. Solid and dot lines in (b) represent bulk extractable
852 and whole-rock compositions respectively. Data from (b) is extracted from Li et al. (2019).
853 REE concentration of the upper continental crust is extracted from Rudnick and Gao (2003).
854
855 **Figure 14**. Relations between proportion of halloysite and kaolinite and clay-adsorbed HREE
856 and LREE concentrations.
857
858 **Figure 15**. Variations of bulk extractable and clay-adsorbed REE concentrations for (a) <2 μm
859 and (b) 2 - 20 μm fractions in different soil horizons. Data for the bulk extractable REE
860 concentrations is extracted from Li et al. (2019).
861

Table 1. Summary of bulk mineralogical and geochemical properties of the Zudong deposit

Soil horizon	Proportion of kaolinite group mineral (%)[1]	Soil pH[1]	Proportion of particle size (%)				Bulk REE concentrartion (ppm)[1]	Proportion of the total REEs (%)[1]			
			<2 μm	2 - 20 μm	20 - 50 μm	>50 μm		Extractable adsorbed REEs	Fe-Mn oxyhydroxide-adsorbed REEs	Fe-Mn oxyhydroxide-bound REEs	Organic substance-bound REEs
Humic layer - Upper pedolith	25	4.74	22.9	57.5	14.8	4.8	394	46	2.5	1.5	0.5
Lower pedolith	12	5.55	11.6	47.6	26.3	14.6	1055	66	2.3	0.8	0.4
Upper saprolite	13	5.40	9.3	37.7	25.1	27.9	906	60	2.1	0.5	0.2
Lower saprolite	10	5.94	8.3	31.1	18.9	41.7	477	61	1.9	0.8	0.5

Remark:
"[1]": Data from Li et al. (2019); analytical methods provided in Appendix

Table 2. Summary of average relative proportions of clay minerals in <2 μm and 2 - 20 μm fractions from different soil horizons

Soil horizon	Size (μm)	Hinckley index*	Kaolinite	Halloysite	Smectite	Interstratified Ms-Ill/Smectite	Muscovite/ Illite	Vermiculite	Interstratified Ms-Ill/Vermiculite
Humic layer - Upper pedolith (n = 4)	<2	0.98	69	2	-	-	6	8	15
	2 - 20	1.83	60	7	-	-	9	6	18
Lower pedolith (n = 2)	<2	0.76	69	23	-	1	1	3	2
	2 - 20	0.33	73	21	-	2	4	-	-
Upper saprolite (n = 3)	<2	0.50	61	33	1	-	4	1	-
	2 - 20	0.89	47	44	1	-	9	-	-
Lower saprolite (n = 3)	<2	0.14	55	36	-	-	3	2	4
	2 - 20	0.29	51	24	-	3	19	1	2

Remarks:
*: Hinckley indices are calculated for the kaolinite-group minerals
-: Not detected
Abbreviation: Ill, illite; Ms, muscovite

Table 3. Summary of average mineralogical, physical and chemical properties of <2 μm and 2 - 20 μm fractions from different soil horizons

Soil horizon	Size (μm)	BET surface area, S_{BET} (m^2/g)	BJH cumulative adsorption surface area, S_{ads} (m^2/g)	BJH cumulative desorption surface area, S_{des} (m^2/g)	S_{ads} - S_{BET}	S_{des} - S_{BET}	Adsorption pore volume (cm^3/g)	Desorption pore volume (cm^3/g)	Cation exchange capacity (c mol/kg^{-1})
Humic layer - Upper pedolith (n = 4)	<2	8.06	8.77	9.59	0.7	1.5	0.06	0.06	15.2
	2 - 20	11.0	12.6	14.3	1.6	3.3	0.05	0.05	11.5
Lower pedolith (n = 3)	<2	15.6	19.0	21.0	3.3	5.3	0.10	0.10	16.6
	2 - 20	12.2	14.6	17.3	2.3	5.1	0.07	0.07	13.2
Upper saprolite (n = 2)	<2	16.7	19.8	23.1	3.1	6.4	0.11	0.11	15.3
	2 - 20	12.5	15.2	18.5	2.7	6.0	0.06	0.06	14.0
Lower saprolite (n = 2)	<2	18.3	20.3	22.2	2.0	3.9	0.12	0.12	13.0
	2 - 20	17.7	21.1	26.5	3.3	8.7	0.07	0.07	11.1

This is a preprint, the final version is subject to change, of the American Mineralogist (MSA)
Cite as Authors (Year) Title. American Mineralogist, in press.
DOI: https://doi.org/10.2138/am-2020-7061

Table 4. Major elemental compositions of the feldspars in the parent rock

	Orthoclase (n = 8)		Albite (n = 9)	
	Average (wt. %)	Range (wt. %)	Average (wt. %)	Range (wt. %)
SiO_2	63.06	62.49 - 64.56	66.97	66.62 - 67.50
TiO_2	b.dl.	b.dl.	b.dl.	b.dl. - 0.02
Al_2O_3	17.48	17.06 - 18.81	18.93	18.62 - 19.41
FeO	0.02	0.01 - 0.04	0.03	b.dl. - 0.05
MnO	b.dl.	b.dl.	b.dl.	b.dl.
MgO	b.dl.	b.dl.	b.dl.	b.dl. - 0.01
CaO	0.02	b.dl. - 0.03	0.40	0.02 - 0.07
Na_2O	0.55	0.26 - 0.83	11.65	10.79 - 12.39
K_2O	16.68	16.13 - 17.56	0.09	0.04 - 0.13
Total	97.81	97.10 - 99.78	98.06	97.50 - 99.21
Si	6.00	5.97 - 6.04	5.98	5.94 - 6.00
Al (IV)	0.01	b.dl. - 0.01	0.02	b.dl. - 0.06
$\sum_{TET}$	6.01	6.00 - 6.04	6.00	6.00
Al (VI)	1.95	1.92 - 2.02	1.97	1.95 - 2.02
Ti	0.00	0.00	0.00	0.00
Fe	0.00	0.00	0.00	0.00
Mn	0.00	0.00	0.00	0.00
Mg	0.00	0.00	0.00	0.00
Ca	0.00	0.00	0.04	0.00. - 0.07
Na	0.10	0.05 - 0.15	2.02	1.87 - 2.14
K	2.02	1.90 - 2.14	0.01	0.00 - 0.01
$\sum_{OCT}$	4.08	3.98 - 4.18	4.04	3.93 - 4.10

Remark: Structural formula of feldspars is calculated on the basis of 16 positive charges

This is a preprint, the final version is subject to change, of the American Mineralogist (MSA)
Cite as Authors (Year) Title. American Mineralogist, in press.
DOI: https://doi.org/10.2138/am-2020-7061

Table 5. Major elemental compositions of the kaolinite group minerals in different soil horizons and muscovite in the parent rock

	Kaolinite group minerals								Muscovite	
	Humic - Upper pedolith (n = 31)		Lower pedolith (n = 26)		Upper saprolite (n = 17)		Lower Saprolite (n = 18)		Parent rock (n = 17)	
	Average (wt. %)	Range (wt. %)	Average (wt. %)	Range (wt. %)	Average (wt. %)	Range (wt. %)	Average (wt. %)	Range (wt. %)	Average (wt. %)	Range (wt. %)
SiO_2	45.13	44.31 - 46.21	45.14	43.78 - 46.41	45.50	44.48 - 46.57	44.86	43.11 - 45.98	45.32	43.37 - 47.02
TiO_2	0.02	b.dl. - 0.52	0.01	b.dl. - 0.11	b.dl.	b.dl. - 0.01	0.03	b.dl. - 0.13	0.05	b.dl. - 0.13
Al_2O_3	38.52	37.17 - 39.76	37.60	28.22 - 39.68	38.42	37.00 - 39.87	37.48	34.50 - 39.41	32.34	29.44 - 36.11
FeO	0.46	0.10 - 1.37	1.57	0.04 - 11.74	0.55	0.06 - 2.02	2.12	0.15 - 5.13	4.53	0.92 - 8.48
MnO	0.01	b.dl. - 0.04	0.04	b.dl. - 0.57	0.02	b.dl. - 0.07	0.02	b.dl. - 0.08	0.40	0.15 - 0.64
MgO	0.07	b.dl. - 0.54	0.17	b.dl. - 0.84	0.03	b.dl. - 0.12	0.18	b.dl. - 1.26	0.12	0.06 - 0.16
CaO	0.07	0.02 - 0.13	0.07	0.03 - 0.12	0.09	0.03 - 0.18	0.08	0.02 - 0.04	0.05	0.02 - 0.07
Na_2O	0.01	b.dl. - 0.04	0.02	b.dl. - 0.22	0.01	b.dl. - 0.05	0.01	b.dl. - 0.05	0.12	0.08 - 0.18
K_2O	0.20	b.dl. - 0.82	0.46	b.dl. - 1.83	0.34	b.dl. - 2.05	0.81	0.02 - 2.24	10.70	10.12 - 11.49
F	b.dl.	b.dl.	0.05	b.dl. - 0.85	0.01	b.dl. - 0.05	b.dl.	b.dl.	0.29	b.dl. - 0.86
Cl	0.03	b.dl. - 0.10	0.09	b.dl. - 0.55	0.01	b.dl. - 0.04	0.03	b.dl. - 0.02	0.01	b.dl. - 0.02
H_2O	13.62	13.40 - 13.96	13.55	12.41 - 13.89	13.68	13.34 - 14.03	13.85	13.13 - 13.85	4.20	3.98 - 4.40
O=F,Cl	0.01	0.00 - 0.02	0.04	0.01 - 0.36	0.01	b.dl. - 0.02	0.01	b.dl. - 0.05	0.12	0.00 - 0.36
Total	98.11	96.40 - 100.45	98.74	95.46 - 100.54	98.65	96.49 - 100.75	99.21	97.85 - 100.59	98.00	96.09 - 100.74
Si	3.97	3.89 - 4.02	3.98	3.91 - 4.16	3.99	3.92 - 4.03	3.96	3.86 - 4.04	6.26	6.12 - 6.36
Al (IV)	0.03	0.00 - 0.11	0.03	0.00 - 0.09	0.02	0.00 - 0.08	0.05	0.00 - 0.14	1.74	1.64 - 1.88
$\sum_{TET}$	4.00	4.00 - 4.02	4.01	4.00 - 4.16	4.00	4.00 - 4.02	4.00	4.00 - 4.04	8.00	8.00
Al (VI)	3.96	3.87 - 4.00	3.88	3.11 - 4.00	3.95	3.84 - 4.00	3.85	3.66 - 3.99	3.53	3.18 - 3.84
Ti	0.00	0.00 - 0.03	0.00	0.00 - 0.01	0.00	0.00	0.00	0.00 - 0.01	0.01	0.00 - 0.01
Fe	0.03	0.01 - 0.10	0.12	0.00 - 0.92	0.04	0.00 - 0.15	0.16	0.01 - 0.39	0.53	0.10 - 1.02
Mn	0.00	0.00	0.00	0.00 - 0.05	0.00	0.00 - 0.01	0.00	0.00 - 0.01	0.05	0.02 - 0.08
Mg	0.01	0.00 - 0.07	0.02	0.00 - 0.11	0.00	0.00 - 0.02	0.02	0.00 - 0.16	0.02	0.01 - 0.03
$\sum_{OCT}$	4.01	3.97 - 4.05	4.02	3.96 - 4.10	4.00	3.97 - 4.01	4.04	4.00 - 4.13	4.13	3.96 - 4.33
Ca	0.01	0.00 - 0.01	0.01	0.00 - 0.01	0.01	0.00 - 0.02	0.01	0.00 - 0.02	0.01	0.00 - 0.01
Na	0.00	0.00 - 0.01	0.00	0.00 - 0.04	0.00	0.00 - 0.01	0.00	0.00 - 0.01	0.03	0.02 - 0.05
K	0.02	0.00 - 0.09	0.05	0.00 - 0.21	0.04	0.00 - 0.23	0.09	0.00 - 0.26	1.89	1.79 - 1.97
$\sum_{EXT}$	0.03	0.00 - 0.10	0.06	0.01 - 0.22	0.05	0.00 - 0.26	0.10	0.01 - 0.28	1.92	1.83 - 2.02

Remark: Structural formula of kaolinite group mineral is calculated on the basis of 14 positive charges and muscovite of 22 positive charges

This is a preprint, the final version is subject to change, of the American Mineralogist (MSA)
Cite as Authors (Year) Title. American Mineralogist, in press.
DOI: https://doi.org/10.2138/am-2020-7061

Table 6. Extraction results of the clay fractions from different soil horizons

Soil horizon	Size fraction (μm)	Extractable pool	REE	LREE	HREE	$(La/Yb)_N$	Ce/Ce*	Eu/Eu*
Humic layer	<2	Clay-adsorbed	277	108	169	0.69	1.46	0.05
		Residual	200	76	123	0.61	2.02	0.05
	2 - 20	Clay-adsorbed	73	26	47	0.58	1.44	0.06
		Residual	255	53	202	0.30	1.57	0.04
Upper pedolith	<2	Clay-adsorbed	1229	239	990	0.63	0.18	0.04
		Residual	363	127	237	0.64	1.84	0.04
	2 - 20	Clay-adsorbed	65	22	43	0.58	1.96	0.05
		Residual	539	97	442	0.36	1.57	0.07
Lower pedolith	<2	Clay-adsorbed	3698	649	3049	0.71	0.03	0.04
		Residual	579	150	429	0.41	2.07	0.04
	2 - 20	Clay-adsorbed	3272	616	2656	0.85	0.02	0.03
		Residual	588	63	525	0.13	2.12	0.02
Upper saprolite	<2	Clay-adsorbed	2613	326	2287	0.46	0.05	0.02
		Residual	634	131	503	0.12	11.8	0.01
	2 - 20	Clay-adsorbed	2355	315	2040	0.50	0.03	0.02
		Residual	601	64	537	0.04	9.07	0.01
Lower saprolite	<2	Clay-adsorbed	1045	177	868	0.66	0.05	0.03
		Residual	350	94	256	0.30	4.12	0.02
	2 - 20	Clay-adsorbed	1062	182	880	0.70	0.04	0.04
		Residual	451	54	397	0.09	3.34	0.01

Remark: all elemental compositions in ppm

This is a preprint, the final version is subject to change, of the American Mineralogist (MSA)
Cite as Authors (Year) Title. American Mineralogist, in press.
DOI: https://doi.org/10.2138/am-2020-7061

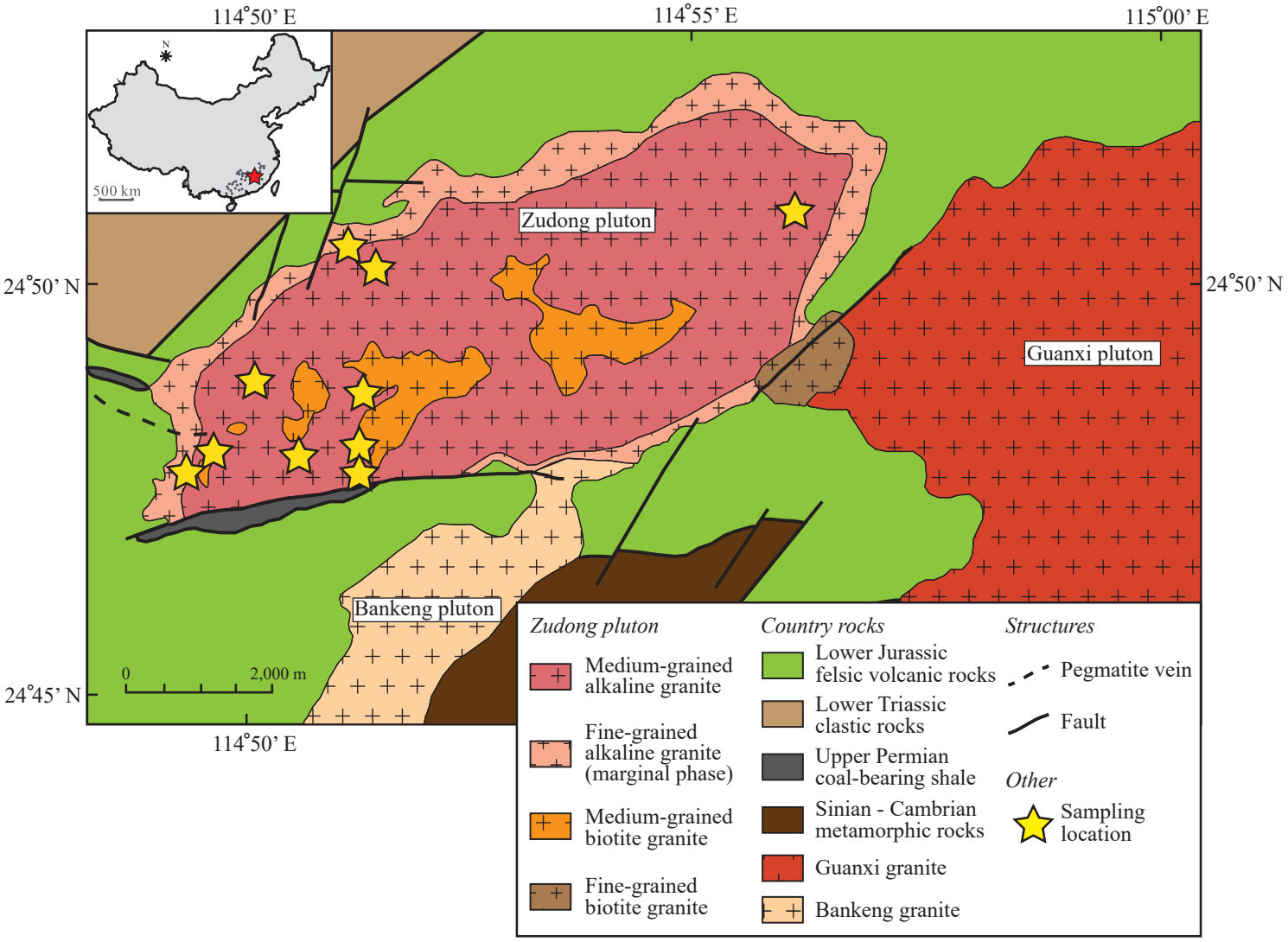

Figure 1

This is a preprint, the final version is subject to change, of the American Mineralogist (MSA)
Cite as Authors (Year) Title. American Mineralogist, in press.
DOI: https://doi.org/10.2138/am-2020-7061

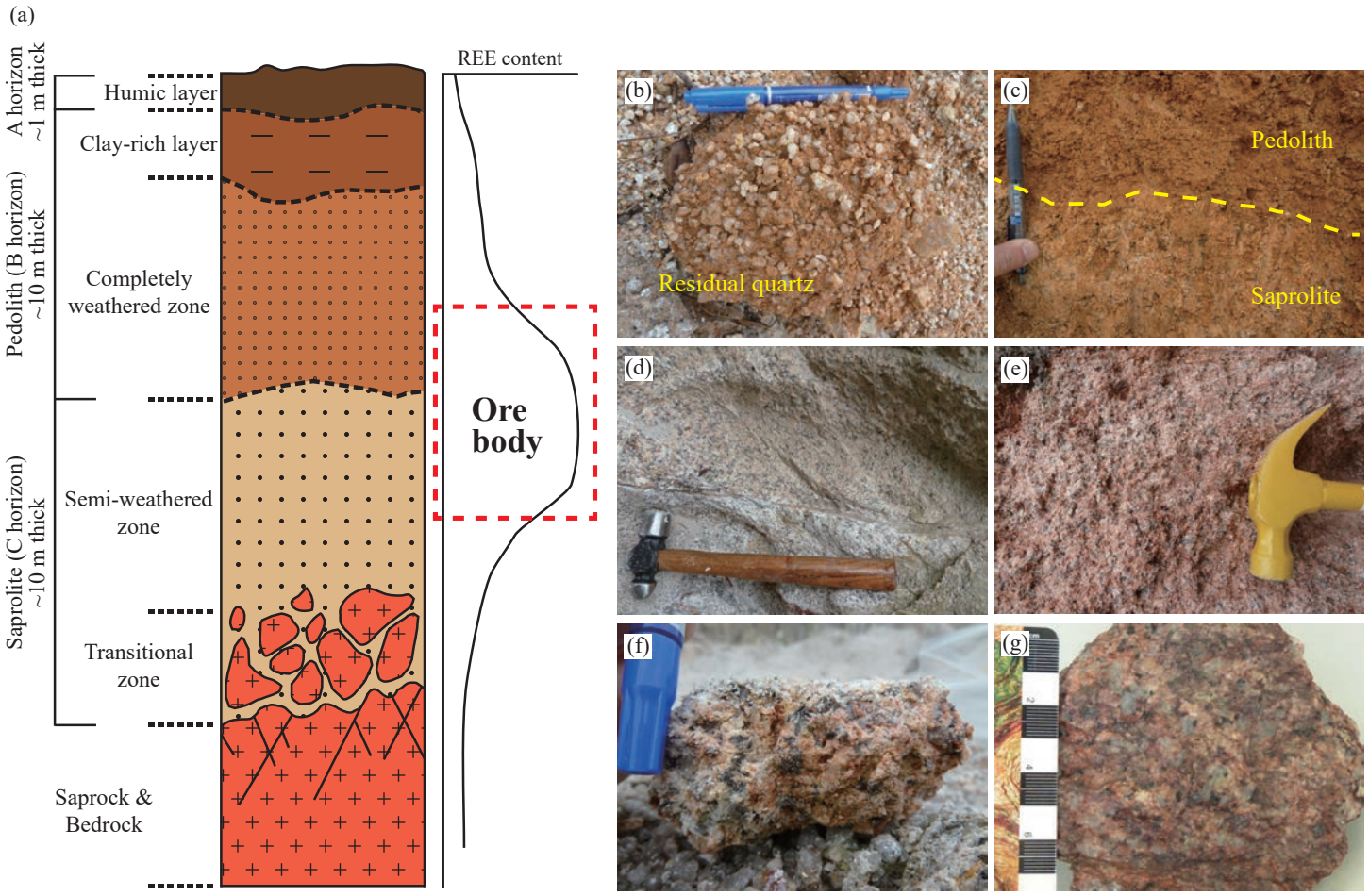

Figure 2

This is a preprint, the final version is subject to change, of the American Mineralogist (MSA)
Cite as Authors (Year) Title. American Mineralogist, in press.
DOI: https://doi.org/10.2138/am-2020-7061

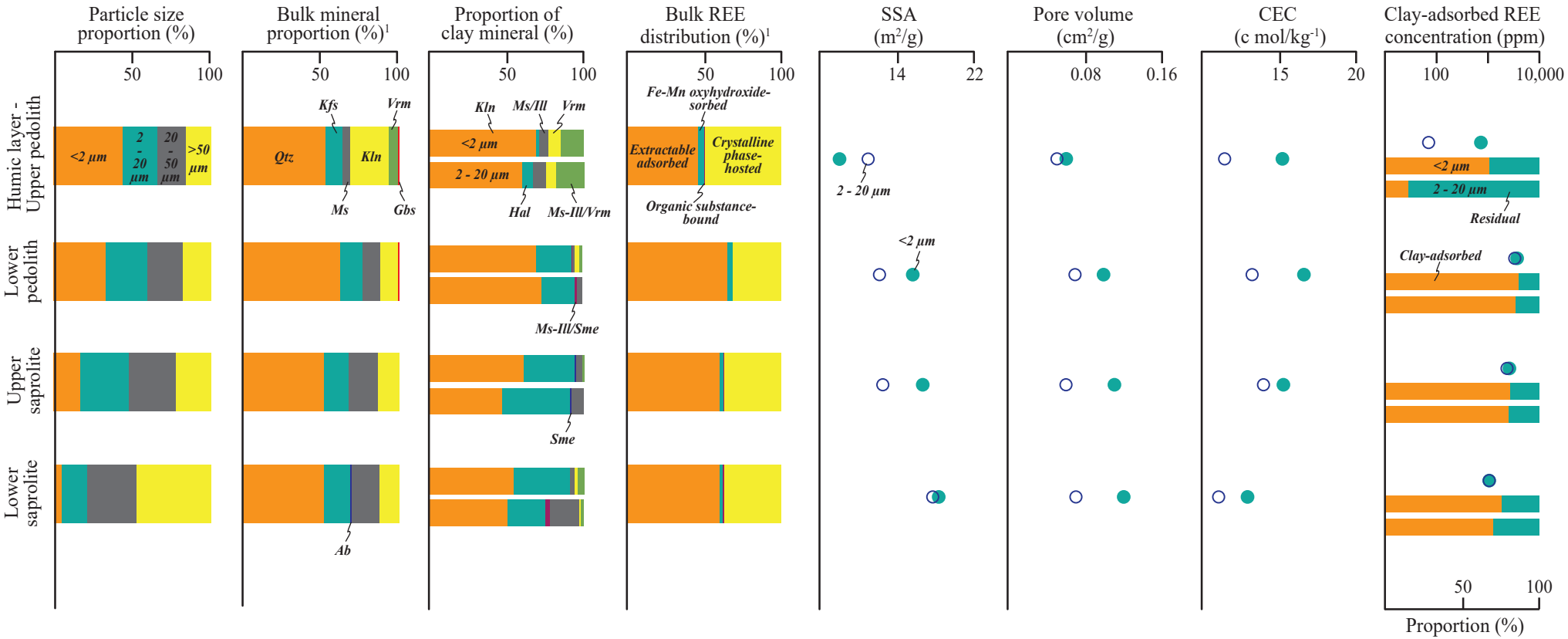

Figure 3

This is a preprint, the final version is subject to change, of the American Mineralogist (MSA)
Cite as Authors (Year) Title. American Mineralogist, in press.
DOI: https://doi.org/10.2138/am-2020-7061

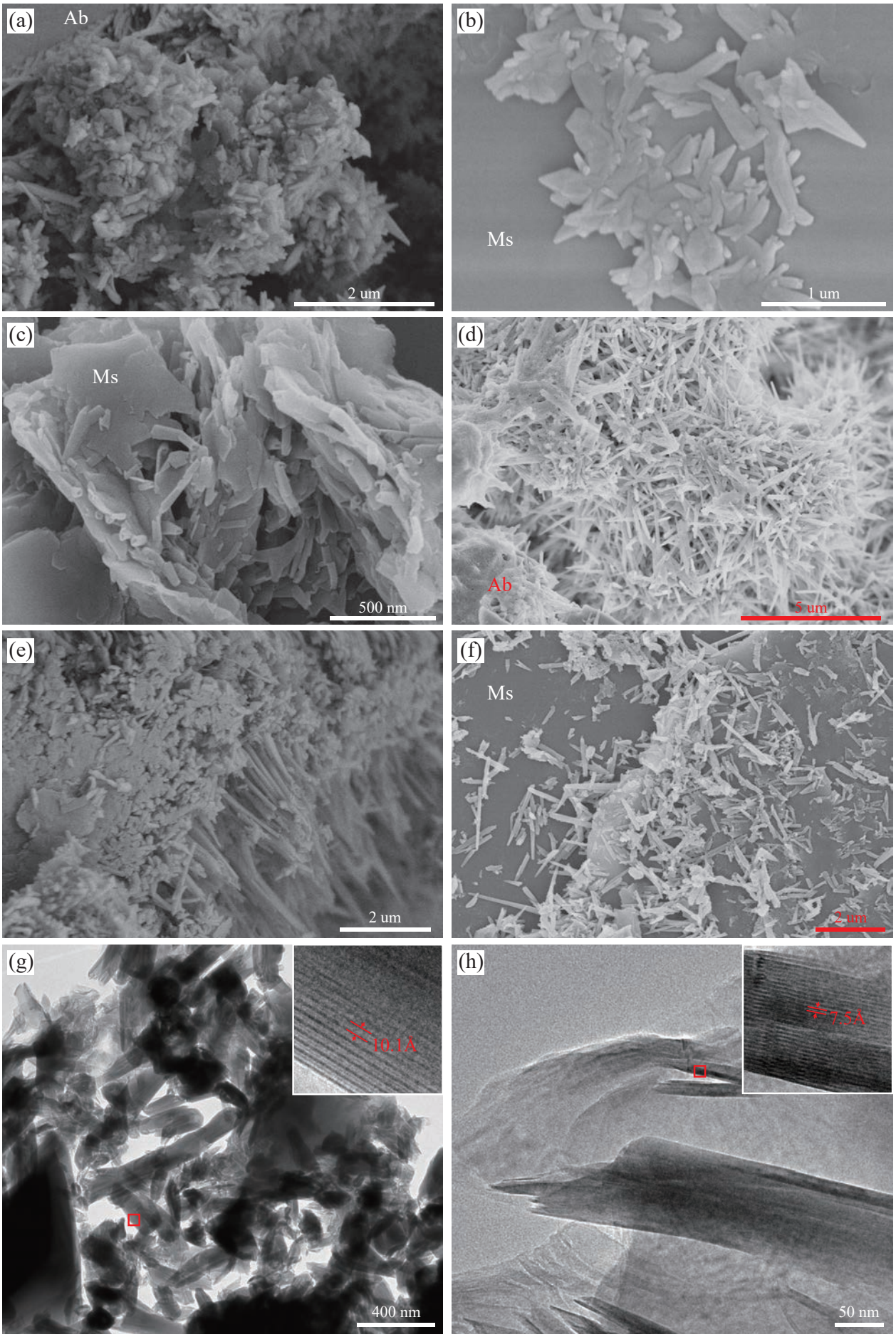

Figure 4

This is a preprint, the final version is subject to change, of the American Mineralogist (MSA)
Cite as Authors (Year) Title. American Mineralogist, in press.
DOI: https://doi.org/10.2138/am-2020-7061

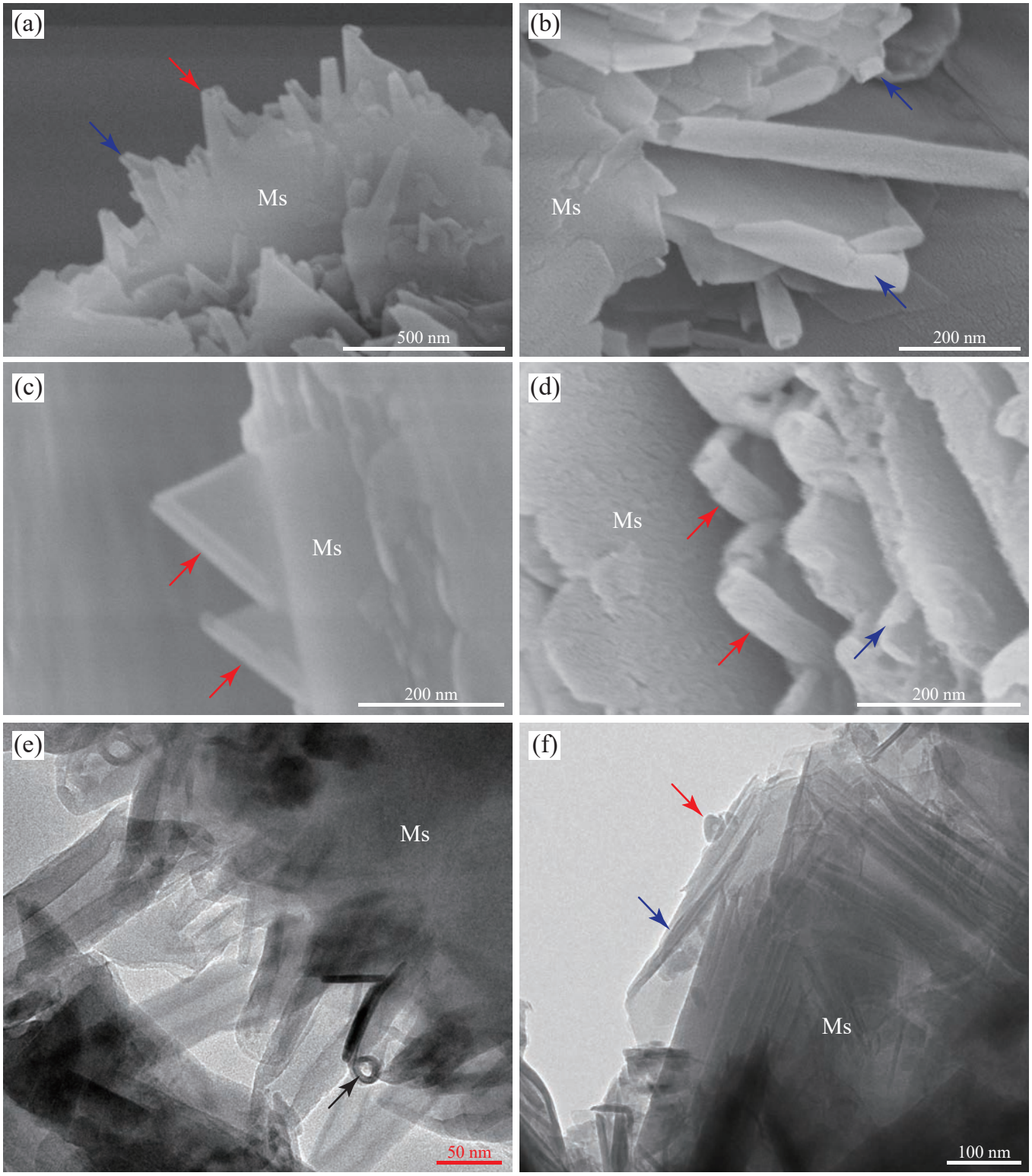

Figure 5

This is a preprint, the final version is subject to change, of the American Mineralogist (MSA)
Cite as Authors (Year) Title. American Mineralogist, in press.
DOI: https://doi.org/10.2138/am-2020-7061

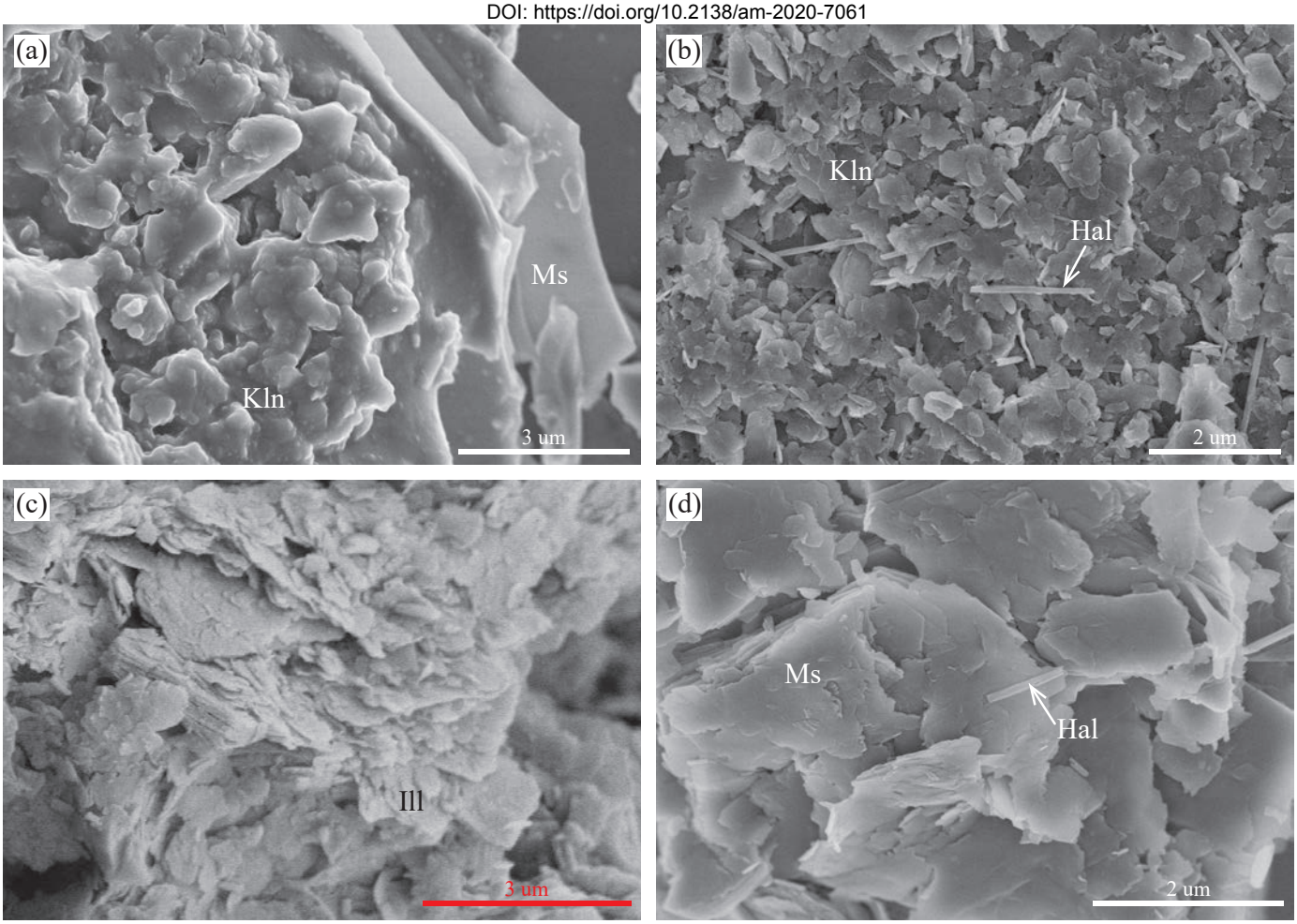

Figure 6

This is a preprint, the final version is subject to change, of the American Mineralogist (MSA)
Cite as Authors (Year) Title. American Mineralogist, in press.
DOI: https://doi.org/10.2138/am-2020-7061

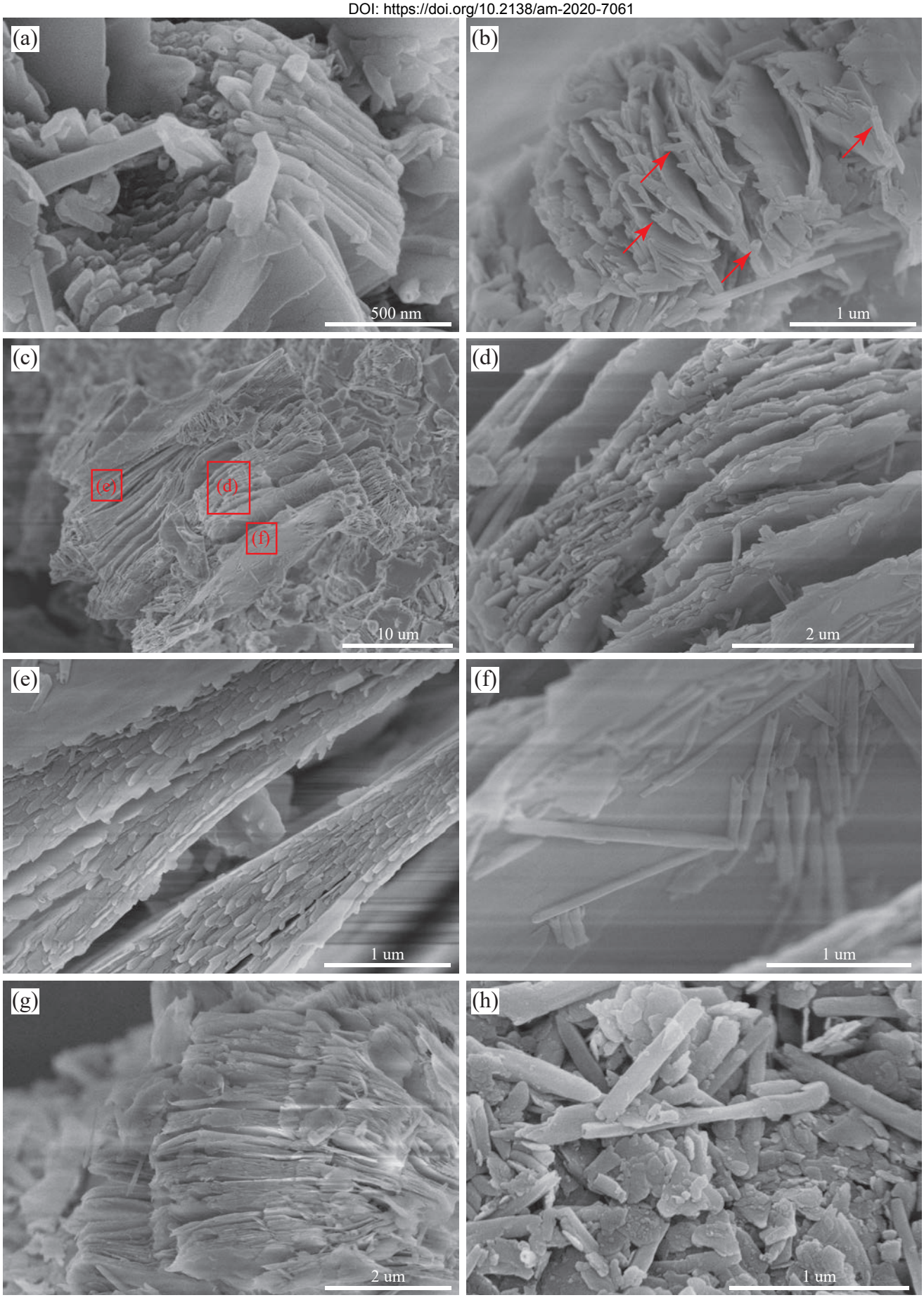

Figure 7

This is a preprint, the final version is subject to change, of the American Mineralogist (MSA)
Cite as Authors (Year) Title. American Mineralogist, in press.
DOI: https://doi.org/10.2138/am-2020-7061

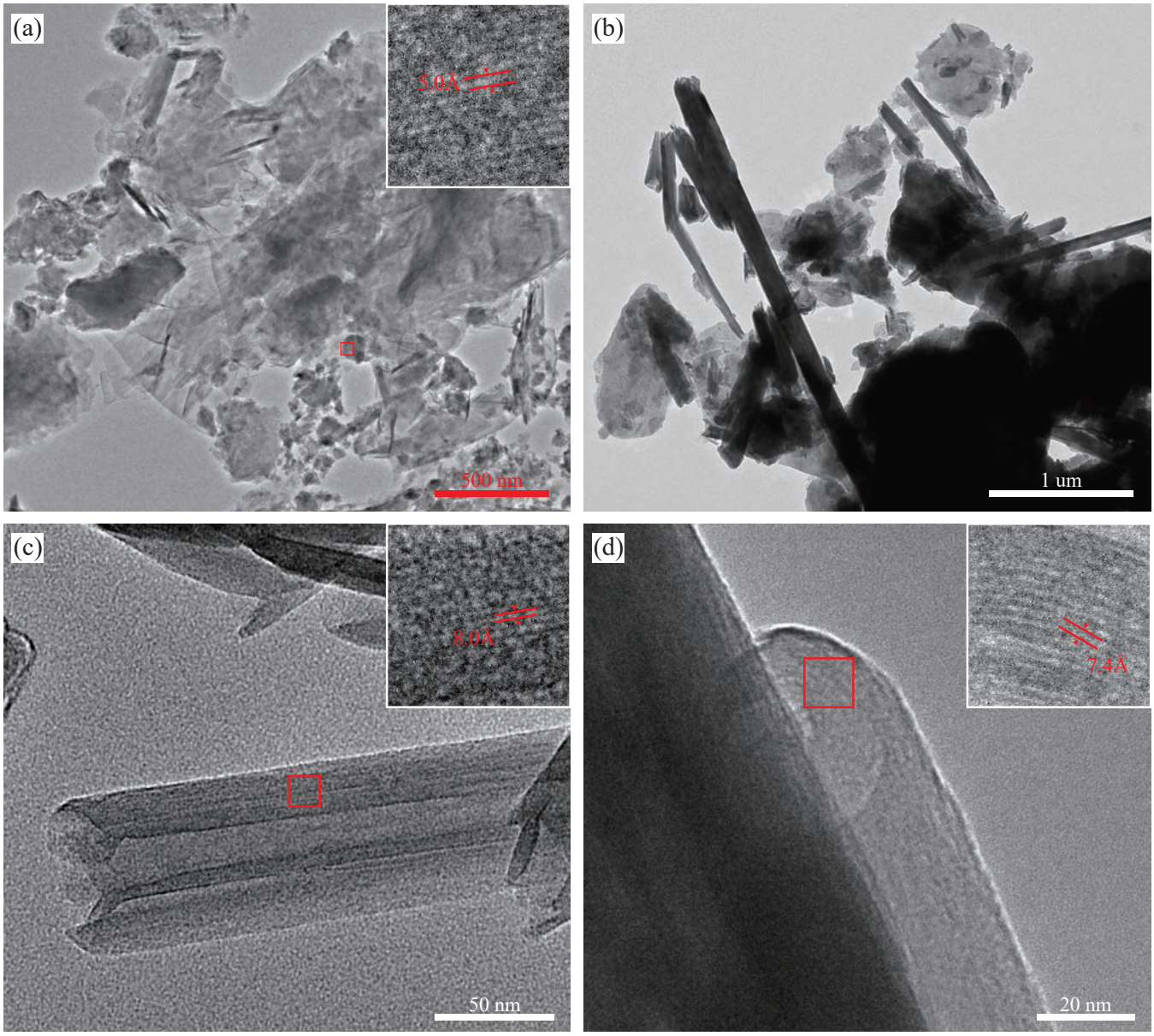

Figure 8

This is a preprint, the final version is subject to change, of the American Mineralogist (MSA)
Cite as Authors (Year) Title. American Mineralogist, in press.
DOI: https://doi.org/10.2138/am-2020-7061

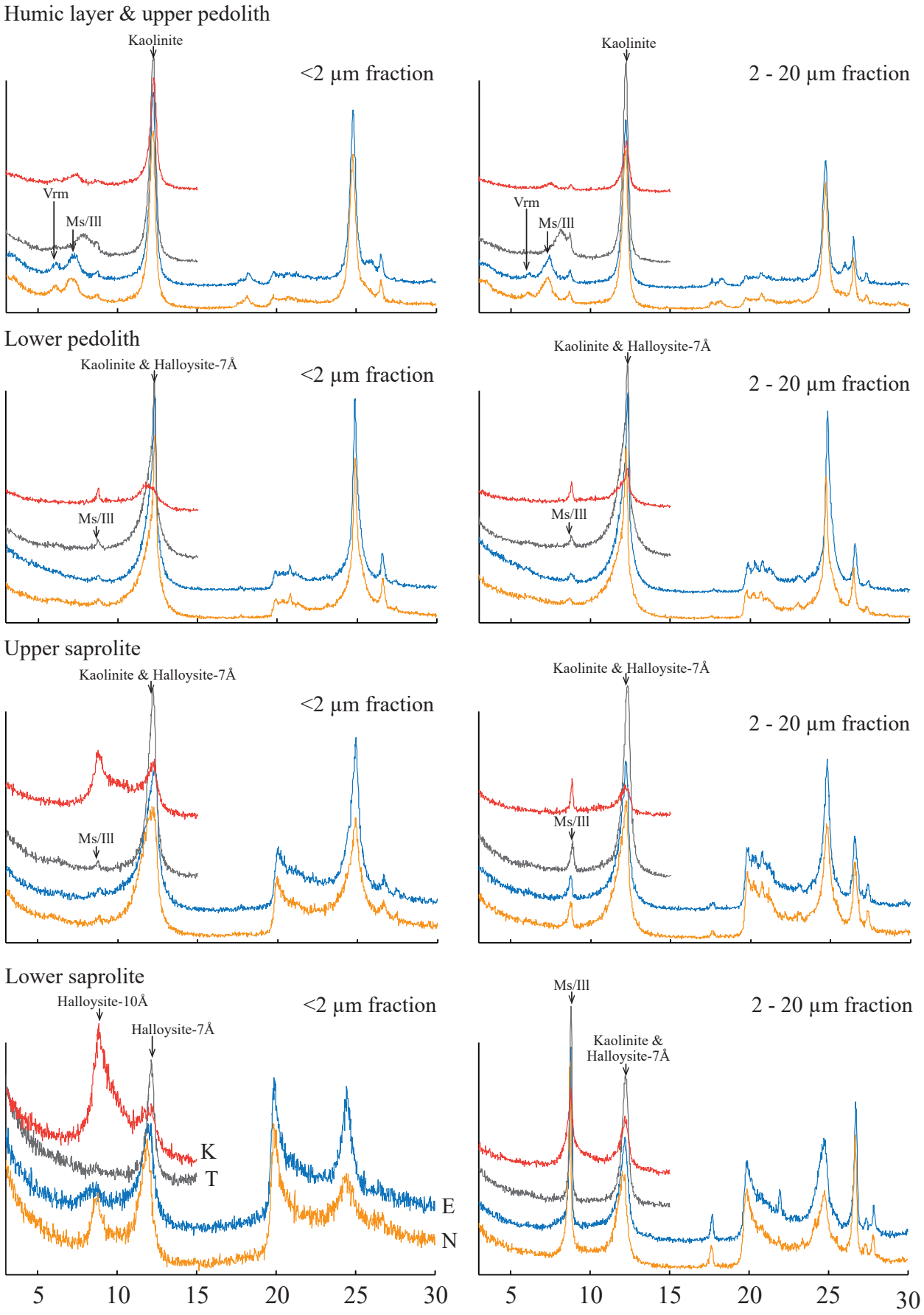

Figure 9

This is a preprint, the final version is subject to change, of the American Mineralogist (MSA)
Cite as Authors (Year) Title. American Mineralogist, in press.
DOI: https://doi.org/10.2138/am-2020-7061

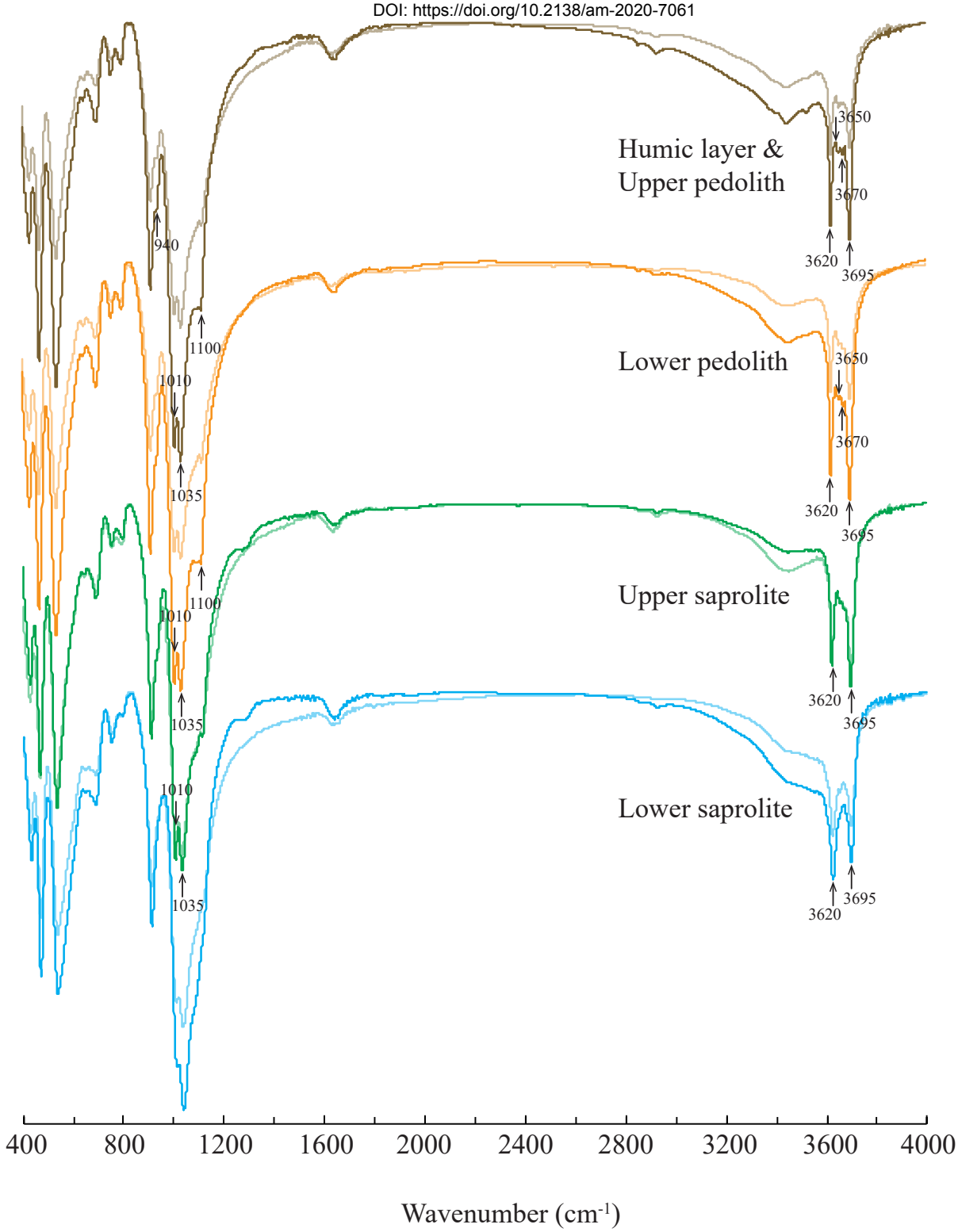

Figure 10

This is a preprint, the final version is subject to change, of the American Mineralogist (MSA)
Cite as Authors (Year) Title. American Mineralogist, in press.
DOI: https://doi.org/10.2138/am-2020-7061

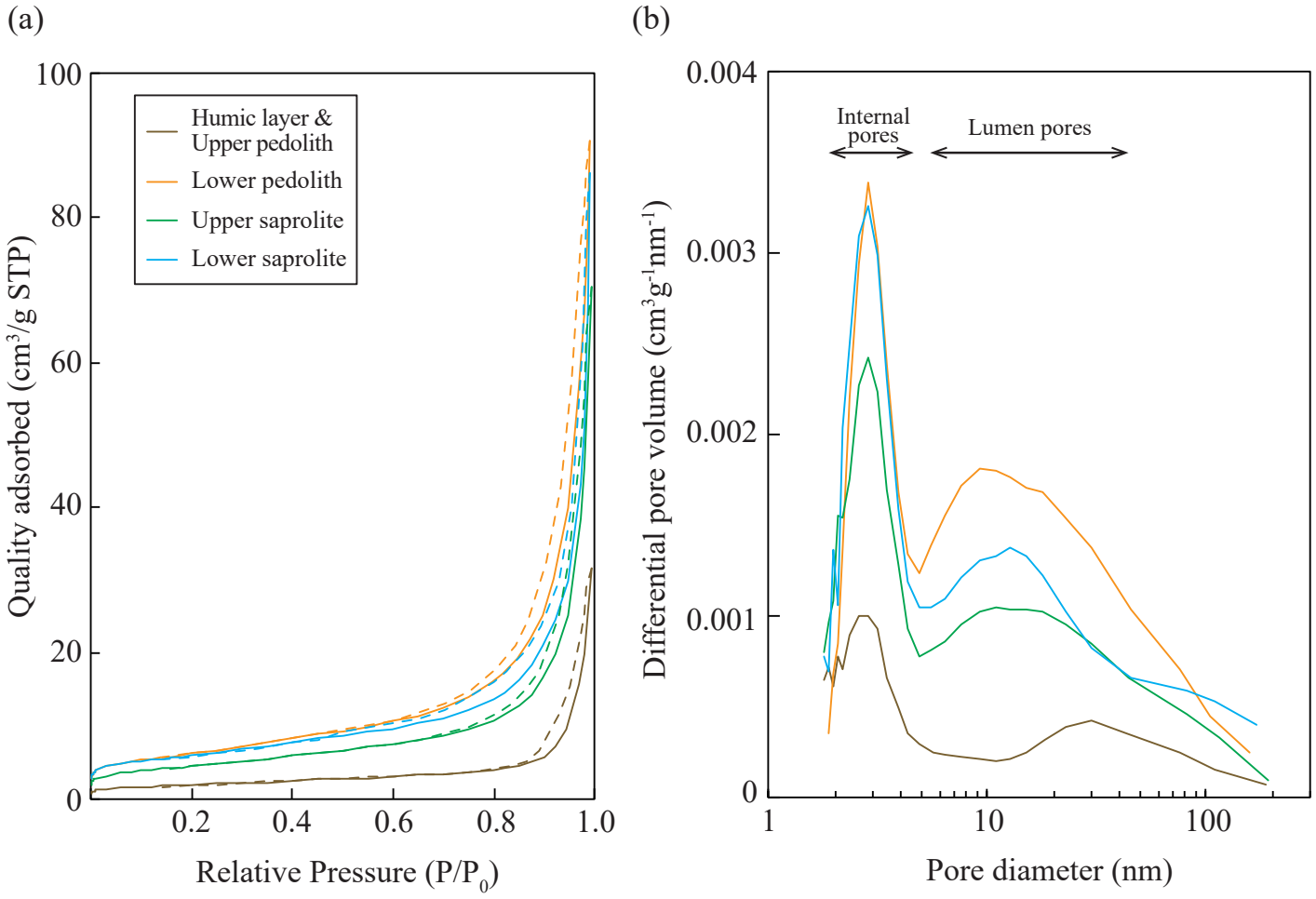

Figure 11

This is a preprint, the final version is subject to change, of the American Mineralogist (MSA)
Cite as Authors (Year) Title. American Mineralogist, in press.
DOI: https://doi.org/10.2138/am-2020-7061

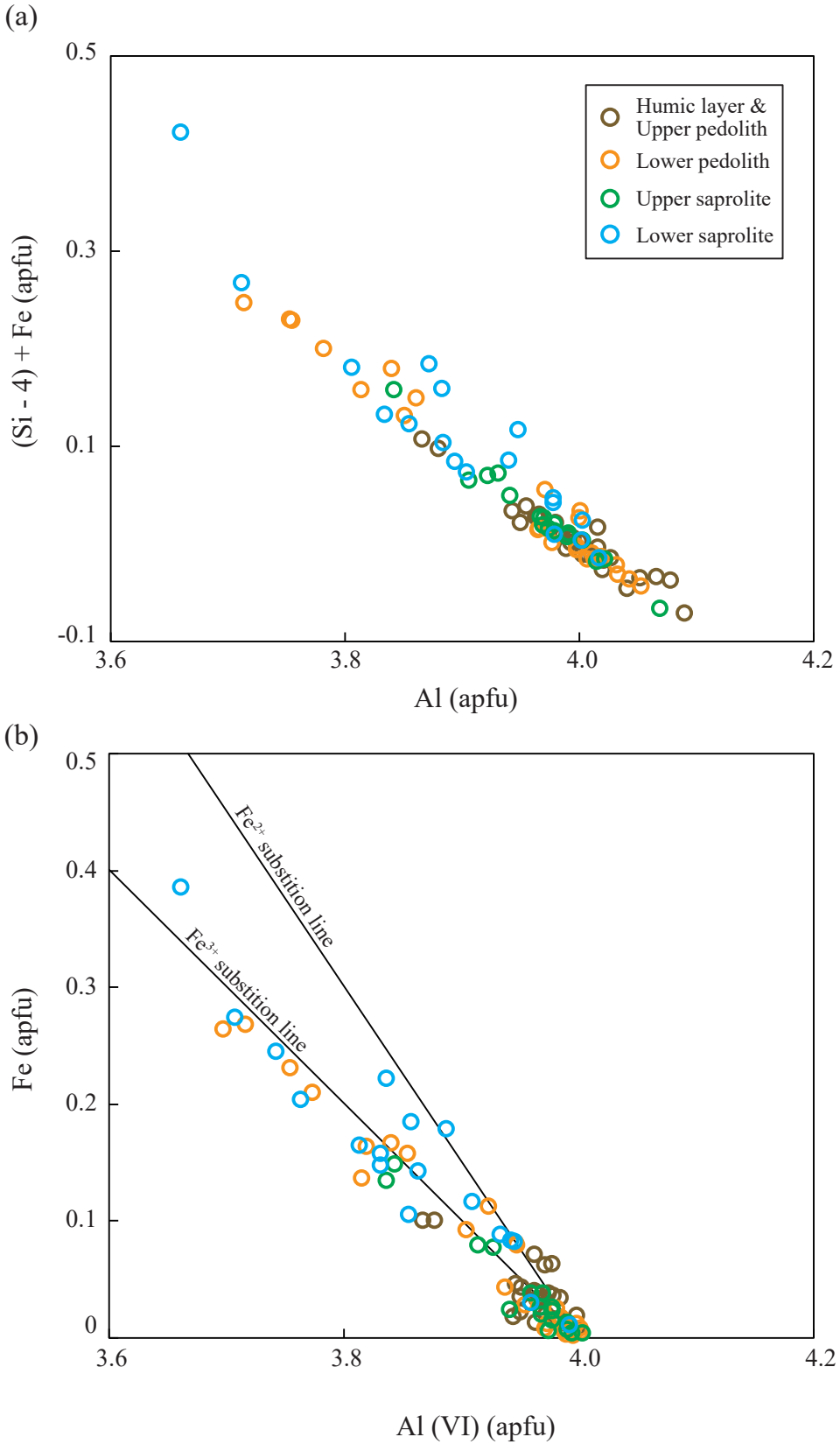

Figure 12

This is a preprint, the final version is subject to change, of the American Mineralogist (MSA)
Cite as Authors (Year) Title. American Mineralogist, in press.
DOI: https://doi.org/10.2138/am-2020-7061

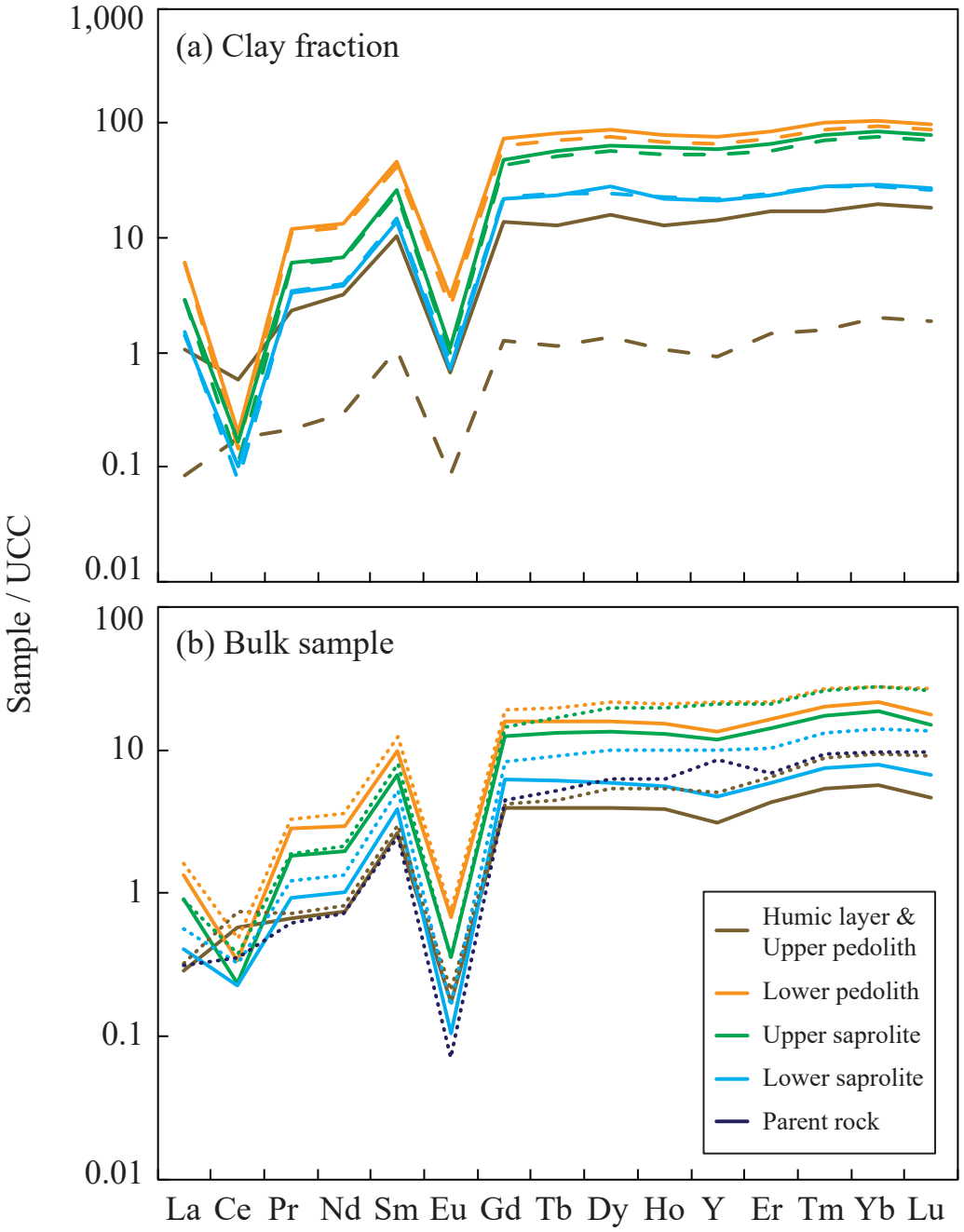

Figure 13

This is a preprint, the final version is subject to change, of the American Mineralogist (MSA)
Cite as Authors (Year) Title. American Mineralogist, in press.
DOI: https://doi.org/10.2138/am-2020-7061

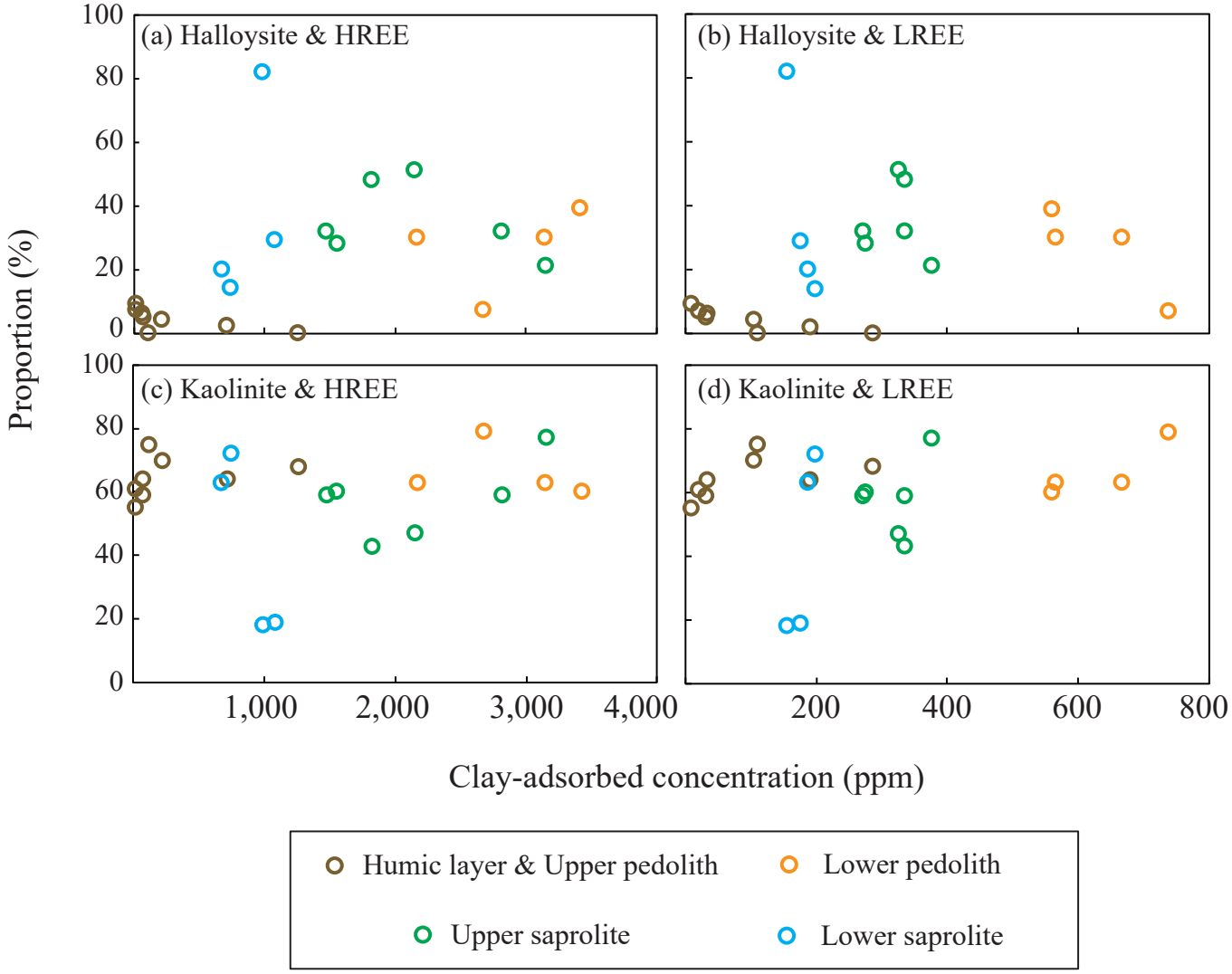

Figure 14

This is a preprint, the final version is subject to change, of the American Mineralogist (MSA)
Cite as Authors (Year) Title. American Mineralogist, in press.
DOI: https://doi.org/10.2138/am-2020-7061

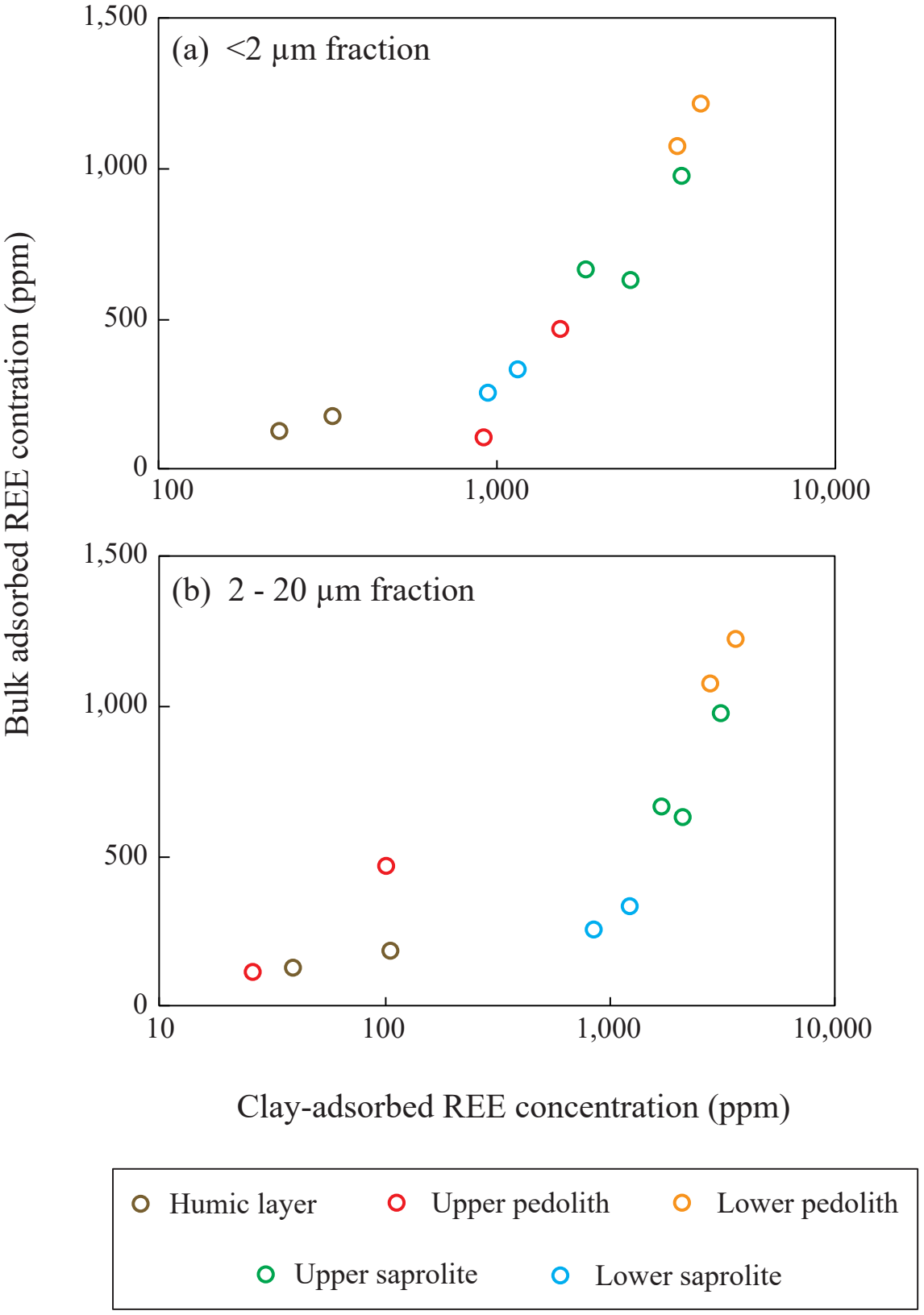

Figure 15